

The LABOCA survey of the *Extended Chandra Deep Field-South* – radio and mid-infrared counterparts to submillimetre galaxies

A. D. Biggs,^{1,2*} R. J. Ivison,^{2,3} E. Ibar,^{2,3} J. L. Wardlow,⁴ H. Dannerbauer,^{5,6}
Ian Smail,⁴ F. Walter,⁵ A. Weiß,⁷ S. C. Chapman,⁸ K. E. K. Coppin,⁴ C. De Breuck,¹
M. Dickinson,⁹ K. K. Knudsen,¹⁰ V. Mainieri,¹ K. Menten⁷ and C. Papovich¹¹

¹European Southern Observatory, Karl Schwarzschild Strasse 2, D-85748 Garching, Germany

²UK Astronomy Technology Centre, Royal Observatory, Blackford Hill, Edinburgh EH9 3HJ

³Institute for Astronomy, University of Edinburgh, Blackford Hill, Edinburgh EH9 3HJ

⁴Institute for Computational Cosmology, Durham University, Durham DH1 6LE

⁵Max-Planck-Institut für Astronomie, Königstuhl 17, D-69117 Heidelberg, Germany

⁶Laboratoire AIM Paris Saclay, CEA-CNRS-Université, Ifu/Service d'Astrophysique, CEA Saclay, Orme de Merisiers, 91191 Gif-sur-Yvette Cedex, France

⁷Max-Planck-Institut für Radioastronomie, Auf dem Hügel 69, D-53121 Bonn, Germany

⁸Institute of Astronomy, Madingley Road, Cambridge CB3 0HA

⁹National Optical Astronomy Observatory, 950 N. Cherry Ave., Tucson, AZ 85719, USA

¹⁰Argelander Institut für Astronomie, Auf dem Hügel 71, D-53121 Bonn, Germany

¹¹Department of Physics, Texas A&M University, College Station, TX 77843-4242, USA

Accepted 2010 November 30. Received 2010 November 30; in original form 2010 February 11

ABSTRACT

We present radio and infrared (3.6–24 μm) counterparts to submillimetre galaxies (SMGs) detected in the *Extended Chandra Deep Field-South* with the Large APEX Bolometer Camera (LABOCA) 870- μm bolometer camera on the 12-m Atacama Pathfinder Experiment. Using the Very Large Array at 1.4 GHz and *Spitzer*, we have identified secure counterparts to 79 of the 126 SMGs [signal-to-noise ratio (S/N) > 3.7, $S_{870} > 4.4$ mJy] in the field, 62 via their radio and/or 24- μm emission, the remainder using a colour-flux cut on Infrared Array Camera 3.6- and 5.8- μm sources chosen to maximize the number of secure, coincident radio and 24- μm counterparts. In constructing our radio catalogue, we have corrected for the effects of ‘flux boosting’, then used the corrected flux densities to estimate the redshifts of the SMGs based on the radio/submm spectral indices. The effect of the boosting correction is to increase the median redshift by 0.2 resulting in a value of $\bar{z} = 2.2_{-0.8}^{+0.7}$ (1σ errors) for the secure radio counterparts, in agreement with other studies, both spectroscopic and photometric.

Key words: galaxies: formation – galaxies: starburst – cosmology: observations – early Universe.

1 INTRODUCTION

Although rare today, ultraluminous infrared galaxies – galaxies with infrared (IR) luminosities exceeding $10^{12} L_{\odot}$ – were extremely common in the early Universe, signposting systems undergoing intense, dust-obscured star formation. Moreover, they contribute a significant fraction of the submillimetre (submm) background (Fixsen et al. 1998). This important high-redshift population was first discovered in the form of bright submm sources behind massive, lensing clusters (Smail, Ivison & Blain 1997) and in blank fields (e.g. Barger et al. 1998; Hughes et al. 1998; Eales et al. 1999), using the Submm Common User Bolometer Array (SCUBA; Holland

et al. 1999) on the 15-m James Clerk Maxwell Telescope (JCMT); a number of surveys with a variety of instruments have now brought the number of known submm galaxies (SMGs) to several hundred (e.g. Coppin et al. 2006; Bertoldi et al. 2007; Greve et al. 2008; Scott et al. 2008).

Cross-identifying the submm sources with emission at other wavelengths is made difficult by the poor spatial resolution of even the largest submm telescopes. For example, the combination of JCMT and SCUBA resulted in a resolution of 14 arcsec (FWHM) at 850 μm . The best way to overcome this would be with mm/submm interferometric observations – capable of locating the submm emission directly, with arcsec accuracy (e.g. Downes et al. 1999; Gear et al. 2000; Iono et al. 2006; Wang et al. 2007; Younger et al. 2007; Ivison et al. 2008; Cowie et al. 2009). Such observations, however, require a large investment of observing time with the few existing

*E-mail: abiggs@eso.org

facilities that are capable, although the advent of the Atacama Large Millimeter/Submillimeter Array (ALMA) will make this strategy much easier in the future.

In the meantime, attaining higher resolution is possible using radio interferometric and IR observations, where the empirical correlations between the far-IR and radio wavebands (Condon 1992) or the bolometric IR/mid-IR (Elbaz et al. 2002) make it much easier to identify the submm emitter, particularly given the low source densities in the radio (Ivison et al. 1998, 2000, 2002; Smail et al. 2000; Dannerbauer et al. 2004). This work has typically relied on data from the Very Large Array (VLA) at 1.4 GHz and *Spitzer* using the 24- μm channel of the MIPS instrument (Rieke et al. 2004; Werner et al. 2004). In addition, high-redshift SMGs can be identified through their IR colours as measured by *Spitzer's* Infrared Array Camera (IRAC) camera (e.g. Pope et al. 2006).

Here we present radio, mid-IR (24 μm) and IRAC counterparts to the 126 SMGs that have been detected in the Large APEX Bolometer Camera (LABOCA) *Extended Chandra Deep Field-South* (ECDF-S) Submm Survey (LESS), a deep blank-field 870- μm survey, down to a 3.7σ limit of 4.4 mJy (Weiß et al. 2009). The ECDF-S is an exceptional area for multiwavelength, wide-field studies of galaxy evolution due to deep X-ray (Giacconi et al. 2001; Lehmer et al. 2005; Luo et al. 2008), optical (Giavalisco et al. 2004; Beckwith et al. 2006), IR (Dickinson et al., in preparation) and radio (Miller et al. 2008; Ivison et al. 2010) data. The CDF-S portion of the field has also been surveyed (Scott et al. 2010) with the AzTEC 1.1-mm bolometric camera (Wilson et al. 2008) on the Atacama Submillimeter Telescope Experiment.

The paper is organized as follows. In Section 2 we describe the submm, radio, 24 μm and IRAC data that have been used to identify counterparts to the submm sources, with particular emphasis on the techniques used to extract source fluxes and positions from the radio map. Section 3 contains details of our counterpart identification strategy, and in Sections 4 and 5 we present lists of the likely counterparts and their properties. Section 6 discusses these results in detail, ascertaining the effectiveness of our strategy. We also derive the redshift distribution of the radio-detected robust counterparts using the radio-submm spectral index relation of Carilli & Yun (1999, 2000) before drawing our conclusions in Section 7. In an appendix, we present detailed notes on some of the sources as well as multiwavelength maps with the counterparts marked.

We assume a flat Λ cold dark matter (ΛCDM) cosmology of $\Omega_\Lambda = 0.73$, $\Omega_m = 0.27$ and $H_0 = 70.5 \text{ km s}^{-1} \text{ Mpc}^{-1}$ (Hinshaw et al. 2009).

2 OBSERVATIONS, REDUCTION AND ANALYSIS

2.1 APEX 870- μm catalogue

LABOCA (Siringo et al. 2009) is a 295-element bolometer camera operating at the 12-m Atacama Pathfinder Telescope (APEX)¹ in the exceptionally dry environment of the Atacama desert in Chile (Güsten et al. 2006). The LESS map comprises 200 h of on-sky integration (excluding overheads) and has extremely uniform noise

coverage (average rms = 1.2 mJy beam⁻¹) over the $30 \times 30 \text{ arcmin}^2$ extent of the ECDF-S, with a resolution of 19 arcsec (FWHM). The catalogue of submm sources identified by LESS is described in detail by Weiß et al. (2009). The full catalogue comprises 126 sources above 3.7σ with a false-detection expectation of ≈ 5 . This is based on extensive simulations as described in Weiß et al. (2009).

2.2 VLA 1.4-GHz catalogue

To identify the radio counterparts to the LESS SMGs, we use the VLA 1.4-GHz map of Miller et al. (2008) which we briefly describe here. The map is constructed from six separate pointings arranged in a hexagonal pattern, centred on the coordinates $03^{\text{h}}32^{\text{m}}28^{\text{s}}$, $-27^{\circ}48'30''$ (J2000). Each pointing consists of approximately eight separate ~ 5 h observations. The noise in the final $34 \times 34 \text{ arcmin}^2$ mosaic is $\sim 6.5 \mu\text{Jy beam}^{-1}$ at its deepest. All data were taken in ‘A’ configuration, resulting in a synthesized beam with dimensions $2.8 \times 1.6 \text{ arcsec}^2$, aligned north–south. When looking for radio counterparts to the SMGs, we do not use the Miller et al. (2008) catalogue as this is truncated at a signal-to-noise ratio (S/N) of 7; instead, we have created our own catalogue containing sources down to an S/N of 3.

Seven of the SMGs in the LESS catalogue lie outside the $34 \times 34 \text{ arcmin}^2$ area of the radio map. For these, we use our own reduction of the VLA data to search for counterparts. Our map was created in a similar fashion to that of Miller et al. (2008) and achieves an rms just below $7 \mu\text{Jy beam}^{-1}$. The flux density of the brightest of the SMG counterparts has a flux density in the two maps that differs by less than 1 per cent, and thus we are confident that the two maps are tied to the same flux scale.

2.2.1 Source extraction

The first step in producing a catalogue of radio sources is to create a map of the noise across the field. Sources with a peak-flux-density-to-noise ratio (PNR) greater than 5 are detected and removed using the standard AIPS source-extraction code, SAD. The residual image is then inverted and the source extraction process repeated in order to remove ‘sources’ with negative flux – mainly prominent side lobes caused by Gibbs ringing (associated with high-S/N sources) which become increasingly prominent with distance from the phase centre of each pointing. Once all significant sources have been removed, a noise map is created for each pixel by fitting a Gaussian to the histogram of pixel values contained within a surrounding circle of diameter 50 arcsec (using RMSD with OPTYPE = ‘HIST’). Aided by the accurate noise map, we start the source extraction again, this time restricting the fitting to positive sources with a PNR equal to or greater than 3.

To improve the accuracy of our extracted flux densities, we extract sources in two ways. In the vast majority of cases, we assume that the source is unresolved and fix the size of the fitted Gaussian to that of the restoring beam. For those sources that are significantly resolved, we instead allow the size of the Gaussian to vary. The reason for this approach is that allowing the size of unresolved sources to vary often produces cases where the peak flux density is greater than the total, a consequence of its measured size being smaller than the beam. The result is that the measured flux densities are less accurate than if their sizes had been held fixed at the width of the restoring beam. We have simulated this effect by injecting multiple point sources into our residual map and extracting them, as with the real map, first with the source size unconstrained, then

¹ This publication is based on data acquired with the APEX under program IDs 078.F-9028(A), 079.F-9500(A), 080.A-3023(A) and 081.F-9500(A). APEX is a collaboration between the Max-Planck-Institut für Radioastronomie, the European Southern Observatory and the Onsala Space Observatory.

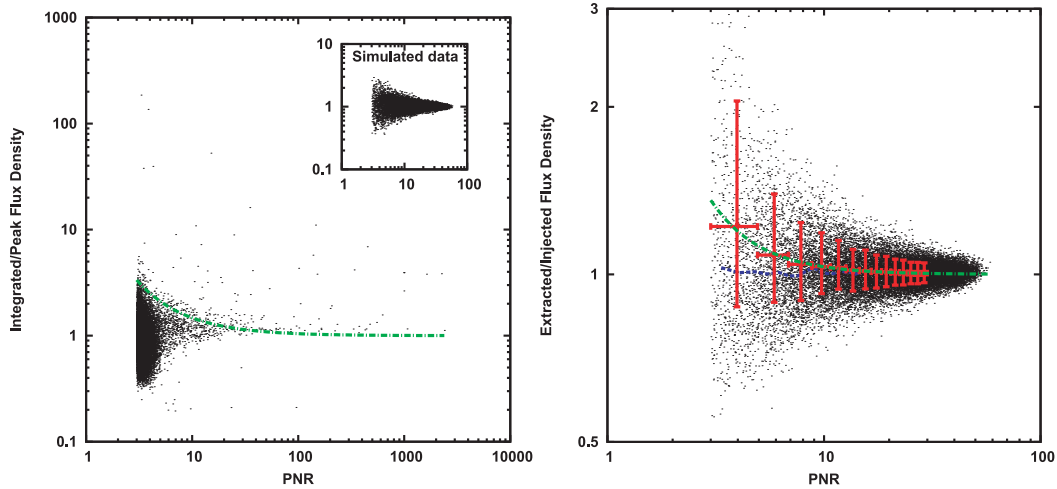


Figure 1. Left: plots of the ratio of the extracted integrated and peak flux densities for simulated sources as a function of PNR. The inset shows the results for simulated point sources and demonstrates how at low S/N the ratio deviates symmetrically from its initial value of unity. The main plot shows the same for the real data along with the upper envelope derived from the simulated data. All sources below the green line were fitted as point sources. Right: ratio of the injected and extracted flux densities for simulated sources as a function of PNR. The points with error bars plot the median gain weighted by the differential source counts (see text) in consecutive bins. The vertical error bars give the range including 68 per cent of the sources in that bin. The dot-dashed line is a polynomial fit to the points and is used to correct the flux densities of the real sources for flux boosting. The lower line shows the median gain without weighting by the source counts – its value is approximately equal to one, independent of PNR.

again with the size fixed to that of the beam. The scatter in the ratio of injected and extracted flux densities was significantly reduced in the latter case (see also Ibar et al. 2009). In all the radio source simulations described in this section, we created 50 fake maps, each containing 500 sources, i.e. a total of 25 000 sources.

In order to use this approach, it is obviously necessary to decide which sources are unresolved and which are resolved. We do this in the following way. When the source size is allowed to vary, the uncertainties in the fitting process cause the ratio of peak to total flux density to increase from unity as often (and by as much) as it decreases; this symmetry is illustrated using our simulated data in the inset of Fig. 1. Each point represents a source injected with the same size as the synthesized beam, but which has increased or decreased in size upon being extracted. The envelope of this plot locates sources in the real data which are inherently unresolved and which should be fitted as such, yielding a more accurate flux density. A similar approach was adopted by Bondi et al. (2003), but using the observed data only and not simulations. Fig. 1 also shows the envelope (containing 98 per cent of the simulated sources) plotted over the real data. Those sources lying above the upper envelope are fitted using a variable width; all other sources are constrained to be point sources.

2.2.2 Bias correction

We have also studied the effects of biases in the model fitting by comparing the fluxes that we recover from our simulations to those that were injected. A plot of this flux density ratio against PNR (calculated based on the *recovered* peak flux, a measure against which we can correct our data) is also shown in the right-hand panel of Fig. 1 (lower line) – we find that the median value is close to unity, independent of PNR i.e. there is no bias in the measured flux densities. This is in contrast to the findings of Seymour, McHardy & Gunn (2004), who find a significant positive bias. This is because Seymour et al. plot their flux ratios as a function of *input* flux density, a quantity which is unknown in the real radio data and which is

biased towards sources whose flux densities have increased due to the model-fitting uncertainties.

2.2.3 Flux boosting

‘Flux boosting’ is an effect regularly taken into account when estimating the flux densities of SMGs (e.g. Coppin et al. 2006; Austermann et al. 2009; Weiß et al. 2009), but very rarely with radio sources. The apparent flux density of such a source deviates from its true value if it sits on/in a noise peak/trough. Because faint sources are more numerous than bright ones, the measured flux density of a catalogued source (i.e. a source lying above the chosen S/N threshold) is more likely to have been boosted than reduced. The most likely flux density is produced by ‘deboosting’ the measured flux densities by the appropriate factor.

We have measured the magnitude of the flux boosting as a function of recovered peak flux density by using the same simulations that were used to investigate the biases in the model fitting. These were performed using equal numbers of sources per flux density bin and therefore do not show the effects of flux boosting (the dots in the right-hand panel of Fig. 1). The source counts can however be added retrospectively by defining flux density bins and again forming a median, but this time weighting each point (source) in a bin by its differential source count (dN/dS). Using our catalogue, we measured a Euclidean slope for the source counts, based on sources above a flux density of $100 \mu\text{Jy}$. This should be valid for all sources fainter than this limit as extremely deep radio observations have shown that there is no change in the slope of the counts down to flux densities as low as $\sim 15 \mu\text{Jy}$ (Owen & Morrison 2008). The bins and the value of the flux boosting correction in each are overplotted on the unweighted data in the right-hand panel of Fig. 1 as red points with error bars; the flux boosting at any value of PNR is calculated by fitting a function to these points (also shown in the figure). For a 3σ source, the flux boosting is equal to 36 per cent.

2.3 *Spitzer* MIPS catalogues

The 24- μm data are taken from the Far-Infrared Deep Extragalactic Legacy Survey (FIDEL; Dickinson et al., in preparation), a programme to map the ECDF-S (as well as the Extended Groth Strip and GOODS-N) at 24 μm using the MIPS camera on board *Spitzer*. The FIDEL MIPS data were reduced following the procedures given in Chary et al. (2004), Frayer et al. (2006) and Frayer et al. (2009). The final image depth at 24 μm varies across the field, with typical exposure times ranging from 11 000 to 30 000 s (with a maximum of approximately 36 000 s). The 24- μm image almost completely covers the area mapped by LABOCA and only one submm source (LESS046) falls off its edge.

For the counterpart analysis, we have used a catalogue produced by the DAOPHOT package from IRAF; the source extraction was not guided by information on positions from other wavelengths. Examination of the differential number counts in the 24- μm data shows that these turn over at $\sim 30 \mu\text{Jy}$ due to incompleteness; thus we have not considered sources with fluxes lower than this. The flux errors reported by the DAOPHOT software are gross underestimates, but simulations have shown that the values of S/N reported by the APEX point-source extraction software specifically developed for *Spitzer* (Makovoz et al. 2002) are accurate. Although we have not used the APEX catalogue for our counterpart analysis (it does not go as deep as that produced using DAOPHOT), matching sources from the two catalogues to within 1 arcsec shows that the APEX S/N and DAOPHOT flux/ Δ flux measurements are linearly related and that the latter need to be multiplied by a factor of 3; the simulations also showed that the flux measurements from each catalogue were consistent.

2.4 *Spitzer* IRAC catalogues

The *Spitzer* IRAC (Fazio et al. 2004) images are taken from the *Spitzer* IRAC and MUSYC Public Legacy in ECDF-S (SIMPLE) survey (Damen et al. 2011). We use SExtractor (Bertin & Arnouts 1996) to extract source positions on a summed image of all four IRAC channels, weighted such that a source of a given magnitude in each image is equally represented. The areas within 15 arcsec of each LESS source were checked visually to ensure the catalogues were complete. We then use APPHOT in IRAF to extract fluxes in 3.8-arcsec diameter apertures on the 3.6- and 5.8- μm images, and apply aperture corrections as derived by the *Spitzer* Wide-area Infrared Survey (SWIRE) team (Surace et al. 2005) to obtain total source magnitudes.

3 IDENTIFYING COUNTERPARTS TO SMGS

Following several other authors (e.g. Ivison et al. 2002, 2007; Pope et al. 2006; Chapin et al. 2009a), we have identified the most likely radio and 24- μm counterparts to the LESS sources by calculating the *corrected Poissonian probability* (Browne & Cohen 1978; Downes et al. 1986) of radio and 24- μm sources that lie within a search radius, r_s , of each SMG. Given a potential counterpart at radius, r , with flux density, S , we can calculate the a priori probability, p , of finding at least one object within that radius of at least that flux density from the expected number of events:

$$\mu_r = \pi r^2 n_S, \quad (1)$$

where n_S is the surface density of sources with fluxes $>S$. The probability is

$$p = 1 - \exp(-\mu_r). \quad (2)$$

However, as the search is being conducted over the (generally) larger radius r_s , this is not the probability we require, i.e. searching at random locations will find more sources as extreme as the one found than would be expected given its measured probability, p . Having found a source of probability p , at radius r , we need to know the number of similar events that would be found in our random search out to r_s . Provided that $p \ll 1$, this is given by

$$\mu_{\text{cor}} = p \left[1 + \ln \left(\frac{p_c}{p} \right) \right], \quad (3)$$

where the so-called critical probability is defined as

$$p_c = \pi r_s^2 n_{\text{lim}} \quad (4)$$

and n_{lim} is the source surface density at our lowest detectable flux density.² The final probability of a counterpart being a chance coincidence is calculated by inserting the corrected number of events (μ_{cor}) into equation (2) in place of μ . As has been typical in the literature (Ivison et al. 2002, 2007; Pope et al. 2006; Chapin et al. 2009a), we take a value of $p \leq 0.05$ to indicate a secure association.

Offsets between the SMG and radio/24- μm sources will be dominated by the uncertainty in the SMG positions, this being a function of the S/N of the submm detection. Therefore, in contrast to some studies of this type that use a search radius based on some representative S/N, we have chosen a different search radius for each SMG that is some multiple of its 1σ positional uncertainty in right ascension/declination ($\approx 1\text{--}3$ arcsec); Smail et al. (2000) similarly used an S/N-dependent search radius. Effects such as telescope pointing errors might conspire to produce systematic offsets between the submm source and its counterpart, but as the final map is an average of multiple observations taken at different times, any such systematic offsets are minimal. Greve et al. (2010) come to the same conclusion from a stacking analysis of the LESS data which confirms the absolute astrometry of the submm map.

In choosing a value for r_s , our overriding concern has been to make it large enough to avoid missing significant numbers of counterparts, but small enough to avoid choosing counterparts from unrelated, bright field sources; too large a radius also overestimates the value of p . A reasonable maximum value for r_s is 3σ as this will ensure that we only miss the counterpart for 1 per cent of the SMGs³ i.e. 1.3 sources. The number of SMGs with missed counterparts is plotted in Fig. 2 over a wide function of radius, 0– 5σ . Also plotted in Fig. 2 are the numbers of secure counterparts found as a function of radius for both the radio and 24- μm catalogues. Both rise steeply between 0 and 2σ and gently decline above $\sim 3\sigma$. We have therefore set our search radius to $r_s = 3\sigma$.

We have also used Monte Carlo simulations to investigate the effect of varying the search radius, producing 100 realizations of the SMG catalogue at radii between 0 and 5σ in steps of 0.5σ and searching for secure counterparts in the same way as with the real data. Each simulated catalogue has the same distribution of flux densities, and therefore search radii, as the real catalogue, but with randomized positions. The results are again shown in Fig. 2 and illustrate that the number of false detections is approximately constant beyond $r_s \sim 1.5\sigma$.

² The critical probability corresponds to finding the faintest possible source at the largest possible distance. By definition, there is no possibility of finding other sources that are at least as probable anywhere else within r_s and so such sources do not require a correction factor, i.e. the factor in square brackets in equation (3) is unity.

³ From the cumulative distribution function (CDF) of the Rayleigh distribution, $\text{CDF} = 1 - e^{-r^2/2\sigma^2}$, where $r_s/\sigma = 3$.

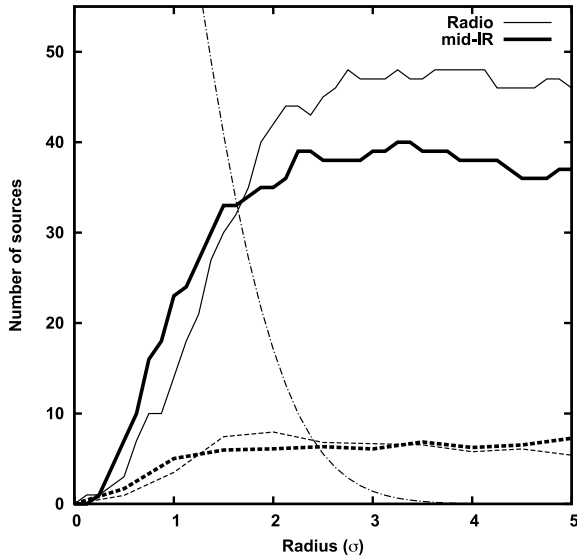


Figure 2. The solid lines show the number of secure counterparts ($p \leq 0.05$) as a function of radius (in units of the SMG 1σ positional uncertainty) for the radio catalogue (thin line) and $24\text{-}\mu\text{m}$ catalogue (thick line). Also shown is the number of SMGs for which the counterpart will not have been found, based on the cumulative distribution function of the Rayleigh distribution (dot-dashed line). The low dashed lines show the results of the Monte Carlo simulations, i.e. the number of secure counterparts found as a function of radius for randomly distributed SMGs. Choosing a radius of 3σ produces close to the maximum number of counterparts and results in only ~ 1 per cent of the SMGs not being searched out to a sufficient radius. Note that we do not show the IRAC IDs here as those were only searched for in error circles devoid of radio and MIPS counterparts, using a selection guided by the radio/MIPS IDs.

The positional errors for each SMG have been determined using the simulated source extractions of Weiß et al. (2009). This offers advantages over analytical formulae such as equation (B22) of Ivison et al. (2007), in that it includes all sources of uncertainty, including those originating in the data reduction and source extraction processes. The empirical formula for the positional uncertainties is

$$\sigma_{x,y} = a \exp(-b S_{\text{in}}) + c, \quad (5)$$

where $a = 6.08$, $b = 0.14$, $c = 0.56$ and S_{in} is the intrinsic flux of the source, i.e. the observed flux after deboosting.

Integrated source counts were calculated for both the radio and $24\text{-}\mu\text{m}$ data from the respective catalogues; these are used to calculate the value of n_S at both the flux density of the potential counterpart and the flux limit (for the radio catalogue, we formed the counts using the undeboosted fluxes as these correspond to the actual source densities in the radio map). In order to test these and the entire p -statistic procedure, we have again performed Monte Carlo simulations, producing 500 realizations of the 126-source submm catalogue as described above. On average, 5 per cent of the SMGs should have a counterpart with $p \leq 0.05$. This corresponds to 6.3 sources on average and we indeed find values of 6.326 for the radio and 6.302 for the $24\text{-}\mu\text{m}$ data. We are thus confident that we are measuring the correct probabilities for each counterpart.

4 THE RADIO AND MIPS COUNTERPARTS

In the following, we try and identify counterparts from the radio and MIPS catalogues. We then use the properties of these counterparts

to select the parameter space in IRAC colour and flux to identify potential counterparts to the radio and MIPS-undetected sources.

The results of our counterpart search are given in Tables 1 (radio) and 2 ($24\text{-}\mu\text{m}$), where we include the position and flux of the counterpart as well as its radial offset from the submm source and the value of the search radius. The first column also gives the ‘ID’ of each SMG, an integer describing the position of each in a ranked list of decreasing S/N (as they appear in each table). For brevity, we will often refer to an individual source using this integer, e.g. LESS001; the integers also refer to the S/N-ranked list in Weiß et al. (2009). Postage stamp maps with a size of $36 \times 36 \text{ arcsec}^2$ centred on the submm position are shown in Fig. A1. We show radio contours superimposed on IRAC $3.6\text{-}\mu\text{m}$ grey-scales. The IRAC images are taken from the SIMPLE Legacy Program (P.I.: P. van Dokkum) and where the SMGs do not lie fully within the SIMPLE coverage, we replace the images with the ones from SWIRE; LESS046 also has its FIDEL image replaced with one from SWIRE. We also show the LESS contours, overplotted on $24\text{-}\mu\text{m}$ grey-scales, in a separate panel.

The criterion for considering a potential counterpart as a secure identification is that $p \leq 0.05$ (Tables 1 and 2). These sources have their values of p given in boldface in Tables 1 and 2, and their positions are marked in Fig. A1. Of the 126 submm sources, 47 have at least one radio and 39 at least one $24\text{-}\mu\text{m}$ counterpart with $p \leq 0.05$; together they produce 60 robust counterparts. Of these, two (LESS063 and LESS118) are extremely weak ($\lesssim 30 \mu\text{Jy}$, deboosted), have low values of p (by virtue of lying very close to the submm position), but do not appear to have associated MIPS or IRAC emission. It is impossible to rule them out as genuine counterparts, but we have highlighted them in Table 1 (p contained within *square* parentheses).

As we have both radio and $24\text{-}\mu\text{m}$ data for most sources, the combination of the results for each SMG enables us to identify additional reliable counterparts. For weak sources, the presence of coincident emission in both wavebands makes it more likely that the source is real, but for any source the presence of emission at radio wavelengths *and* $24\text{-}\mu\text{m}$ makes it more likely that the galaxy is the correct identification. Individual sources with $0.05 < p \leq 0.1$ (i.e. still low enough to indicate a likely counterpart) have their value of p within parentheses, but where coincident radio and $24\text{-}\mu\text{m}$ components have $0.05 < p \leq 0.1$ we consider this to be a secure identification and present the value of p in parenthesized boldface. Two more SMGs gain robust counterparts in this way, LESS036 and LESS060.

In summary, we find statistically robust counterparts to 62 (49 per cent) of the SMGs using the radio and $24\text{-}\mu\text{m}$ data (Table 4). We now go on to extend our sample of identified SMGs by exploiting the very deep IRAC observations of this field.

5 IRAC COUNTERPARTS

To identify counterparts to submm sources without secure radio or MIPS identifications, we employ 3.6- and $5.8\text{-}\mu\text{m}$ *Spitzer* IRAC data. Fig. 3 shows the 3.6- and $5.8\text{-}\mu\text{m}$ colour-flux diagram for sources in the ECDF-S, with secure radio- or MIPS-identified SMG counterparts highlighted. An IRAC counterpart to every MIPS and radio robust identification was found by examining each by eye, taking into account any radio emission and optical sources in the region under consideration (from MUSYC imaging). It is apparent from Fig. 3 that SMGs are typically redder than the field population, and it is this property we will exploit to identify counterparts to some unidentified SMGs.

Table 1. Radio properties of potential counterparts to LESS 870- μm sources in the ECDF-S. SMGs are listed in order of decreasing S/N. SMG names appended with an ****** indicate that they are not on the Miller et al. (2008) map; radio counterparts have instead been searched for using our own reduction. Secure counterparts ($p \leq 0.05$) are in boldface and where p lies between 0.05 and 1.0 this is given in parentheses. Counterparts where $0.05 < p \leq 0.1$ is obtained at two out of radio, 24- μm (Table 2) or 5.8- μm (Table 3) have their value of p given in boldface within parentheses. Counterparts which formally have $p \leq 0.05$ but may be spurious are given in square parentheses. Although not used in the p -statistic procedure, all radio fluxes have been corrected for flux boosting (Section 2.2.3.)

ID	SMG name	Submm position		r_s (arcsec)	Radio position		Radio flux (μJy)	Offset (arcsec)	p
		(α_{J2000})	(δ_{J2000})		(α_{J2000})	(δ_{J2000})			
001	LESS J033314.3–275611	03:33:14.26	–27:56:11.2	3.1	–	–	–	–	–
002	LESS J033302.5–275643	03:33:02.50	–27:56:43.6	3.8	03:33:02.7150	–27:56:42.539	234.6 \pm 7.8	3.0	0.004
003	LESS J033321.5–275520	03:33:21.51	–27:55:20.2	3.8	–	–	–	–	–
004	LESS J033136.0–275439	03:31:36.01	–27:54:39.2	4.1	–	–	–	–	–
005	LESS J033129.5–275907	03:31:29.46	–27:59:07.3	4.6	–	–	–	–	–
006	LESS J033257.1–280102	03:32:57.14	–28:01:02.1	4.8	03:32:56.9734	–28:01:01.204	42.7 \pm 7.4	2.4	0.013
007	LESS J033315.6–274523	03:33:15.55	–27:45:23.6	5.1	03:33:15.4267	–27:45:24.430	75.8 \pm 6.9	1.8	0.006
008	LESS J033205.1–273108*	03:32:05.07	–27:31:08.8	4.0	–	–	–	–	–
009	LESS J033211.3–275210	03:32:11.29	–27:52:10.4	5.1	03:32:11.3737	–27:52:12.139	31.0 \pm 6.3	2.1	0.025
010	LESS J033219.0–275219	03:32:19.02	–27:52:19.4	5.1	03:32:19.0632	–27:52:14.829	54.9 \pm 6.0	4.6	0.035
					03:32:19.1370	–27:52:18.115	51.1 \pm 6.1	2.0	0.011
					03:32:19.3086	–27:52:19.018	50.1 \pm 6.2	3.8	0.029
011	LESS J033213.6–275602	03:32:13.58	–27:56:02.5	5.2	03:32:13.8475	–27:56:00.247	55.1 \pm 6.6	4.2	0.029
012	LESS J033248.1–275414	03:32:48.12	–27:54:14.7	5.3	03:32:47.9995	–27:54:16.497	39.9 \pm 6.5	2.4	0.020
					03:32:48.3987	–27:54:16.741	21.4 \pm 5.5	4.2	0.113
013	LESS J033249.2–274246	03:32:49.23	–27:42:46.6	5.3	–	–	–	–	–
014	LESS J033152.6–280320	03:31:52.64	–28:03:20.4	5.1	03:31:52.4870	–28:03:18.934	89.4 \pm 8.0	2.5	0.007
015	LESS J033333.4–275930	03:33:33.36	–27:59:30.1	5.3	–	–	–	–	–
016	LESS J033218.9–273738	03:32:18.89	–27:37:38.7	5.8	03:32:18.6870	–27:37:43.145	49.0 \pm 8.5	5.2	0.039
017	LESS J033207.6–275123	03:32:07.59	–27:51:23.0	6.1	03:32:07.3105	–27:51:20.849	120.3 \pm 14.5	4.3	0.015
018	LESS J033205.1–274652	03:32:05.12	–27:46:52.1	6.2	03:32:04.9033	–27:46:47.449	130.1 \pm 17.3	5.5	0.020
019	LESS J033208.1–275818	03:32:08.10	–27:58:18.7	6.4	03:32:08.2721	–27:58:14.069	30.8 \pm 6.0	5.2	(0.090)
020	LESS J033316.6–280018	03:33:16.56	–28:00:18.8	6.5	03:33:16.7726	–28:00:16.120	4251.9 \pm 16.0	3.9	0.001
021	LESS J033329.9–273441	03:33:29.93	–27:34:41.7	6.2	–	–	–	–	–
022	LESS J033147.0–273243	03:31:47.02	–27:32:43.0	5.9	03:31:46.9496	–27:32:39.547	111.3 \pm 25.3	3.6	0.009
023	LESS J033212.1–280508	03:32:12.11	–28:05:08.5	5.8	–	–	–	–	–
024	LESS J033336.8–274401	03:33:36.79	–27:44:01.0	6.3	03:33:36.9881	–27:43:58.749	60.0 \pm 8.1	3.5	0.019
025	LESS J033157.1–275940	03:31:57.05	–27:59:40.8	6.8	03:31:56.8845	–27:59:39.653	61.3 \pm 7.3	2.5	0.012
026	LESS J033136.9–275456	03:31:36.90	–27:54:56.1	7.0	–	–	–	–	–
027	LESS J033149.7–273432	03:31:49.73	–27:34:32.7	6.5	–	–	–	–	–
028	LESS J033302.9–274432	03:33:02.92	–27:44:32.6	6.9	–	–	–	–	–
029	LESS J033336.9–275813	03:33:36.90	–27:58:13.0	6.6	03:33:36.8866	–27:58:09.382	44.7 \pm 8.6	3.6	0.024
030	LESS J033344.4–280346	03:33:44.37	–28:03:46.1	5.5	–	–	–	–	–
031	LESS J033150.0–275743	03:31:49.96	–27:57:43.9	7.2	03:31:49.8280	–27:57:40.833	25.9 \pm 5.8	3.5	(0.085)
032	LESS J033243.6–274644	03:32:43.57	–27:46:44.0	7.2	–	–	–	–	–
033	LESS J033149.8–275332	03:31:49.78	–27:53:32.9	7.2	–	–	–	–	–
034	LESS J033217.6–275230	03:32:17.64	–27:52:30.3	7.2	–	–	–	–	–
035	LESS J033110.3–273714*	03:31:10.35	–27:37:14.8	5.9	–	–	–	–	–
036	LESS J033149.2–280208	03:31:49.15	–28:02:08.7	7.2	03:31:48.9740	–28:02:14.399	47.5 \pm 7.5	6.2	(0.057 + MIPS)
037	LESS J033336.0–275347	03:33:36.04	–27:53:47.6	6.9	–	–	–	–	–
038	LESS J033310.2–275641	03:33:10.20	–27:56:41.5	7.5	–	–	–	–	–
039	LESS J033144.9–273435	03:31:44.90	–27:34:35.4	7.3	03:31:45.0493	–27:34:37.060	45.9 \pm 7.5	2.6	0.017
					03:31:45.0634	–27:34:30.112	27.9 \pm 6.7	5.7	(0.105)
040	LESS J033246.7–275120	03:32:46.74	–27:51:20.9	7.6	03:32:46.8465	–27:51:21.024	119.1 \pm 13.7	1.4	0.003
041	LESS J033110.5–275233*	03:31:10.47	–27:52:33.2	6.2	–	–	–	–	–
042	LESS J033231.0–275858	03:32:31.02	–27:58:58.1	7.7	–	–	–	–	–
043	LESS J033307.0–274801	03:33:07.00	–27:48:01.0	7.6	03:33:07.4844	–27:47:59.336	25.2 \pm 6.4	6.6	0.168
044	LESS J033131.0–273238	03:31:30.96	–27:32:38.5	6.9	03:31:31.2272	–27:32:39.111	90.3 \pm 9.6	3.6	0.012
045	LESS J033225.7–275228	03:32:25.71	–27:52:28.5	7.7	03:32:25.2714	–27:52:30.692	31.1 \pm 5.9	6.2	0.135
046	LESS J033336.8–273247	03:33:36.80	–27:32:47.0	6.5	03:33:36.7533	–27:32:49.574	73.2 \pm 10.7	2.6	0.008
047	LESS J033256.0–273317	03:32:56.00	–27:33:17.7	7.2	–	–	–	–	–
048	LESS J033237.8–273202	03:32:37.77	–27:32:02.0	6.8	03:32:38.0090	–27:31:59.927	84.5 \pm 8.3	3.8	0.015
049	LESS J033124.4–275040	03:31:24.45	–27:50:40.9	7.6	03:31:24.2001	–27:50:42.774	31.5 \pm 7.1	3.8	(0.056)
					03:31:24.5046	–27:50:37.576	36.0 \pm 7.2	3.4	0.038
					03:31:24.7140	–27:50:46.507	115.9 \pm 19.1	6.6	0.029
050	LESS J033141.2–274441	03:31:41.15	–27:44:41.5	7.9	03:31:40.9917	–27:44:35.238	77.3 \pm 7.2	6.6	0.047
					03:31:41.4170	–27:44:46.966	38.8 \pm 6.8	6.5	(0.090)
051	LESS J033144.8–274425	03:31:44.81	–27:44:25.1	7.9	03:31:45.0647	–27:44:27.794	29.5 \pm 6.3	4.3	(0.093)

Table 1 – *continued*

ID	SMG name	Submm position		r_s (arcsec)	Radio position		Radio flux (μ Jy)	Offset (arcsec)	p
		(α_{J2000})	(δ_{J2000})		(α_{J2000})	(δ_{J2000})			
052	LESS J033128.5–275601	03:31:28.51	–27:56:01.3	7.9	–	–	–	–	–
053	LESS J033159.1–275435	03:31:59.12	–27:54:35.5	8.0	–	–	–	–	–
054	LESS J033243.6–273353	03:32:43.61	–27:33:53.6	7.6	–	–	–	–	–
055	LESS J033302.2–274033	03:33:02.20	–27:40:33.6	8.0	–	–	–	–	–
056	LESS J033153.2–273936	03:31:53.17	–27:39:36.1	8.1	03:31:53.1189	–27:39:38.555	31.8 ± 6.5	2.5	0.036
057	LESS J033152.0–275329	03:31:51.97	–27:53:29.7	8.0	03:31:51.9370	–27:53:27.179	49.4 ± 6.7	2.6	0.018
058	LESS J033225.8–273306	03:32:25.79	–27:33:06.7	7.6	03:32:25.5399	–27:33:06.953	25.2 ± 6.7	3.3	(0.069)
059	LESS J033303.9–274412	03:33:03.87	–27:44:12.2	8.2	03:33:03.8207	–27:44:14.497	22.1 ± 5.9	2.4	(0.069)
					03:33:03.5906	–27:44:13.586	29.5 ± 6.3	4.0	(0.085)
060	LESS J033317.5–275121	03:33:17.47	–27:51:21.5	8.3	03:33:17.4972	–27:51:28.796	64.7 ± 6.9	7.3	(0.067 + MIPS)
061	LESS J033245.6–280025	03:32:45.63	–28:00:25.3	8.3	–	–	–	–	–
062	LESS J033236.4–273452	03:32:36.41	–27:34:52.5	8.2	03:32:36.5309	–27:34:53.363	151.2 ± 7.3	1.8	0.003
					03:32:36.6933	–27:34:47.261	28.4 ± 6.4	6.5	0.136
063	LESS J033308.5–280044	03:33:08.46	–28:00:44.3	8.3	03:33:08.5591	–28:00:44.866	31.8 ± 7.2	1.4	[0.013]
064	LESS J033201.0–280025	03:32:01.00	–28:00:25.6	8.4	03:32:00.9468	–28:00:26.467	23.6 ± 6.2	1.1	0.018
065	LESS J033252.4–273527	03:32:52.40	–27:35:27.7	8.3	–	–	–	–	–
066	LESS J033331.7–275406	03:33:31.69	–27:54:06.1	8.2	03:33:31.9745	–27:54:10.257	67.0 ± 7.8	5.6	0.041
067	LESS J033243.3–275517	03:32:43.28	–27:55:17.9	8.4	03:32:43.2046	–27:55:14.289	90.1 ± 14.8	3.7	0.018
					03:32:43.8211	–27:55:15.380	25.1 ± 5.8	7.6	0.225
068	LESS J033233.4–273918	03:32:33.44	–27:39:18.5	8.4	03:32:33.9689	–27:39:14.491	20.6 ± 5.5	8.1	0.257
069	LESS J033134.3–275934	03:31:34.26	–27:59:34.3	8.5	–	–	–	–	–
070	LESS J033144.0–273832	03:31:43.97	–27:38:32.5	8.5	03:31:44.0325	–27:38:35.859	322.3 ± 14.6	3.5	0.005
071	LESS J033306.3–273327	03:33:06.29	–27:33:27.7	8.0	–	–	–	–	–
072	LESS J033240.4–273802	03:32:40.40	–27:38:02.5	8.5	03:32:40.0506	–27:38:09.235	34.3 ± 7.1	8.2	0.118
073	LESS J033229.3–275619	03:32:29.33	–27:56:19.3	8.5	03:32:29.3049	–27:56:19.404	18.9 ± 5.1	0.3	0.005
					03:32:29.3518	–27:56:23.802	18.5 ± 5.2	4.5	0.228
074	LESS J033309.3–274809	03:33:09.34	–27:48:09.9	8.4	03:33:09.1492	–27:48:16.833	43.8 ± 7.5	7.4	(0.085 + IRAC)
					03:33:09.3836	–27:48:15.887	34.8 ± 7.0	6.0	(0.095)
075	LESS J033126.8–275554	03:31:26.83	–27:55:54.6	8.4	03:31:27.1942	–27:55:51.287	72.3 ± 8.2	5.9	0.038
076	LESS J033332.7–275957	03:33:32.67	–27:59:57.2	8.4	03:33:32.3411	–27:59:54.831	41.6 ± 8.4	5.0	0.042
077	LESS J033157.2–275633	03:31:57.23	–27:56:33.2	8.8	–	–	–	–	–
078	LESS J033340.3–273956	03:33:40.30	–27:39:56.9	8.4	03:33:40.1122	–27:39:49.684	75.2 ± 9.8	7.6	0.044
079	LESS J033221.2–275623	03:32:21.25	–27:56:23.5	8.8	03:32:21.6159	–27:56:23.755	34.8 ± 6.3	4.9	(0.087)
080	LESS J033142.2–274834	03:31:42.23	–27:48:34.4	8.9	03:31:41.8328	–27:48:36.131	27.6 ± 6.2	5.5	0.148
					03:31:42.8359	–27:48:36.936	47.4 ± 6.6	8.4	0.110
081	LESS J033127.4–274440	03:31:27.45	–27:44:40.4	8.8	03:31:27.5722	–27:44:39.651	217.9 ± 15.3	1.8	0.002
082	LESS J033253.8–273810	03:32:53.77	–27:38:10.9	9.0	–	–	–	–	–
083	LESS J033308.9–280522	03:33:08.92	–28:05:22.0	8.3	–	–	–	–	–
084	LESS J033154.2–275109	03:31:54.22	–27:51:09.8	8.9	03:31:54.5185	–27:51:05.700	33.5 ± 6.1	5.7	0.119
					03:31:54.8325	–27:51:10.973	23.3 ± 5.7	8.2	0.272
085	LESS J033110.3–274503*	03:31:10.28	–27:45:03.1	7.7	–	–	–	–	–
086	LESS J033114.9–274844	03:31:14.90	–27:48:44.3	8.5	–	–	–	–	–
087	LESS J033251.1–273143	03:32:51.09	–27:31:43.0	8.4	03:32:50.8711	–27:31:41.762	128.3 ± 25.8	3.2	0.008
					03:32:51.0736	–27:31:45.730	56.9 ± 8.7	2.7	0.014
088	LESS J033155.2–275345	03:31:55.19	–27:53:45.3	9.0	03:31:54.7502	–27:53:41.012	33.6 ± 6.1	7.2	0.167
					03:31:54.8959	–27:53:41.303	78.0 ± 6.6	5.6	0.042
					03:31:55.7818	–27:53:48.183	35.2 ± 6.0	8.4	0.182
089	LESS J033248.4–280023	03:32:48.44	–28:00:23.8	9.1	–	–	–	–	–
090	LESS J033243.7–273554	03:32:43.65	–27:35:54.1	9.1	–	–	–	–	–
091	LESS J033135.2–274033	03:31:35.25	–27:40:33.7	9.1	–	–	–	–	–
092	LESS J033138.4–274336	03:31:38.36	–27:43:36.0	9.2	–	–	–	–	–
093	LESS J033110.8–275607	03:31:10.84	–27:56:07.2	8.4	–	–	–	–	–
094	LESS J033307.3–275805	03:33:07.27	–27:58:05.0	9.1	–	–	–	–	–
095	LESS J033241.7–275846	03:32:41.74	–27:58:46.1	9.2	03:32:41.2324	–27:58:41.752	34.5 ± 6.6	8.0	0.152
096	LESS J033313.0–275556	03:33:13.03	–27:55:56.8	9.2	03:33:12.6380	–27:55:51.515	80.6 ± 17.4	7.4	(0.058)
097	LESS J033313.7–273803	03:33:13.65	–27:38:03.4	9.2	–	–	–	–	–
098	LESS J033130.2–275726	03:31:30.22	–27:57:26.0	9.3	03:31:29.8979	–27:57:22.733	141.8 ± 8.1	5.4	0.020
099	LESS J033251.4–275536	03:32:51.45	–27:55:36.0	9.2	–	–	–	–	–
100	LESS J033111.3–280006	03:31:11.32	–28:00:06.2	8.8	–	–	–	–	–
101	LESS J033151.5–274552	03:31:51.47	–27:45:52.1	9.3	03:31:51.6370	–27:45:52.262	25.3 ± 6.1	2.2	0.052
102	LESS J033335.6–274020	03:33:35.61	–27:40:20.1	9.2	03:33:36.1277	–27:40:18.677	27.7 ± 7.6	7.0	0.132
103	LESS J033325.3–273400	03:33:25.35	–27:34:00.4	9.2	03:33:25.8532	–27:33:57.591	30.5 ± 8.0	7.3	0.104
104	LESS J033258.5–273803	03:32:58.46	–27:38:03.0	9.4	03:32:57.8327	–27:37:59.389	33.1 ± 6.8	9.1	0.178

Table 1 – continued

ID	SMG name	Submm position		r_s (arcsec)	Radio position		Radio flux (μ Jy)	Offset (arcsec)	p
		(α_{J2000})	(δ_{J2000})		(α_{J2000})	(δ_{J2000})			
105	LESS J033115.8–275313	03:31:15.78	–27:53:13.1	9.0	–	–	–	–	–
106	LESS J033140.1–275631	03:31:40.09	–27:56:31.4	9.4	03:31:40.1985	–27:56:23.051	66.8 ± 7.1	8.5	(0.086)
107	LESS J033130.8–275150	03:31:30.85	–27:51:50.9	9.4	03:31:30.5820	–27:51:45.062	24.6 ± 6.3	6.8	0.204
					03:31:31.3078	–27:51:44.774	30.4 ± 6.8	8.6	0.199
108	LESS J033316.4–275033	03:33:16.42	–27:50:33.1	9.5	03:33:16.5352	–27:50:39.704	379.7 ± 36.4	6.8	0.015
109	LESS J033328.1–274157	03:33:28.08	–27:41:57.0	9.5	03:33:28.0319	–27:42:03.554	24.6 ± 6.6	6.6	0.184
110	LESS J033122.6–275417	03:31:22.64	–27:54:17.2	9.4	03:31:22.7410	–27:54:12.315	36.3 ± 7.9	5.1	(0.064)
111	LESS J033325.6–273423	03:33:25.58	–27:34:23.0	9.4	03:33:25.1978	–27:34:25.322	54.0 ± 9.4	5.6	0.042
112	LESS J033249.3–273112*	03:32:49.28	–27:31:12.3	9.0	03:32:48.8585	–27:31:13.054	29.6 ± 8.0	5.7	(0.081)
					03:32:49.4709	–27:31:19.667	31.0 ± 7.9	7.8	(0.100)
113	LESS J033236.4–275845	03:32:36.42	–27:58:45.9	9.5	–	–	–	–	–
114	LESS J033150.8–274438	03:31:50.81	–27:44:38.5	9.7	03:31:51.1106	–27:44:37.552	95.4 ± 6.7	4.1	0.022
115	LESS J033349.7–274239*	03:33:49.71	–27:42:39.2	8.9	–	–	–	–	–
116	LESS J033154.4–274525	03:31:54.42	–27:45:25.5	9.7	03:31:54.2386	–27:45:27.809	23.0 ± 5.7	3.3	0.119
					03:31:54.4428	–27:45:31.605	39.3 ± 6.2	6.1	(0.104)
117	LESS J033128.0–273925	03:31:28.02	–27:39:25.2	9.7	03:31:27.5941	–27:39:27.989	81.0 ± 8.4	6.3	0.042
118	LESS J033121.8–274936	03:31:21.81	–27:49:36.8	9.7	03:31:21.9425	–27:49:41.894	36.4 ± 6.9	5.4	(0.082)
					03:31:21.8153	–27:49:35.179	23.5 ± 6.3	1.6	[0.032]
119	LESS J033256.5–280319	03:32:56.51	–28:03:19.1	9.7	–	–	–	–	–
120	LESS J033328.4–275655	03:33:28.45	–27:56:55.9	9.8	03:33:28.5832	–27:56:54.376	45.5 ± 8.4	2.3	0.015
					03:33:28.5885	–27:56:58.901	26.0 ± 7.5	3.5	(0.075)
121	LESS J033333.3–273449	03:33:33.32	–27:34:49.3	9.7	03:33:33.0528	–27:34:51.686	29.0 ± 8.2	4.3	(0.062)
					03:33:33.0900	–27:34:42.616	35.6 ± 8.6	7.4	(0.086)
122	LESS J033139.6–274120	03:31:39.62	–27:41:20.4	9.9	03:31:39.5493	–27:41:19.658	207.3 ± 14.5	1.2	0.001
123	LESS J033330.9–275349	03:33:30.88	–27:53:49.3	9.8	–	–	–	–	–
124	LESS J033203.6–273605	03:32:03.59	–27:36:05.0	10.0	03:32:03.1065	–27:36:01.967	41.9 ± 7.5	7.1	(0.095)
					03:32:03.4080	–27:36:08.877	25.1 ± 6.4	4.6	0.125
125	LESS J033146.0–274621	03:31:46.02	–27:46:21.2	9.9	–	–	–	–	–
126	LESS J033209.8–274102	03:32:09.76	–27:41:02.0	9.9	03:32:09.5918	–27:41:07.368	23.3 ± 5.5	5.8	0.230

To decide on our colour and flux selection limits, we exploit the radio- and MIPS-identified SMGs to determine limits which balance completeness and purity. We arbitrarily chose a limit of 10 per cent contamination (within the 3σ search radii of SMGs) and maximize the completeness of recovery. Based upon these requirements, we select SMG counterparts with $\log[S_{5.8\mu\text{m}}(\mu\text{Jy})] \geq 0.75$ and $\log(S_{5.8\mu\text{m}}/S_{3.6\mu\text{m}}) \geq -0.05$, returning 78 per cent of the secure radio and MIPS SMG counterparts. Also shown in Fig. 3 are the colour–magnitude cuts of Pope et al. (2006), the colour division of which separates SMGs into low- and high-redshift samples (SMGs redder than the colour limit correspond to $z > 1.5$).

We apply this colour selection to the 64 error circles of SMGs lacking secure radio or MIPS counterparts and calculate a value of p in a similar way to the radio and 24- μm sources described in Section 3 (Table 3) – Monte Carlo simulations again show that the values of p are reliable. In total, we identify 17 additional SMGs with robust counterparts. Four have multiple robust identifications and in one case (LESS074) the second counterpart results from there being a probable ($0.05 < p \leq 0.1$) in both the IRAC and radio data. With the addition of the IRAC counterparts, a total of 79 (63 per cent) of the SMGs have at least one robust counterpart. The details of the 79 robust counterparts are shown in Table 4, including the deboosted submm, 24 μm and deboosted radio flux densities.

6 ANALYSIS AND DISCUSSION

Before the addition of the IRAC results, compared to some other studies (Ivison et al. 2002, 2005; Pope et al. 2006; Ivison et al. 2007), the fraction of SMGs with a secure identification (49 per

cent) is a little low. For example, in the SCUBA Half-Degree Extragalactic Survey (SHADES; Coppin et al. 2006), 79 out of 120 SMGs (66 per cent) were found to have secure counterparts (Ivison et al. 2007) and in the *Hubble Deep Field-North* (HDF-N) Pope et al. (2006) claim secure counterparts for 60 per cent of their sample. However, the fraction of SMGs with robust counterparts is clearly a function of the sensitivity of the radio and mid-IR data, and we note that in the case of the HDF-N ($5.3 \mu\text{Jy beam}^{-1}$ – Biggs & Ivison 2006) and the Lockman Hole portion of SHADES ($4.2 \mu\text{Jy beam}^{-1}$ – Biggs & Ivison 2006), the radio maps were more sensitive than that in the ECDF-S ($6.5 \mu\text{Jy beam}^{-1}$ – Miller et al. 2008). Assuming no cosmic variance and an integral source count slope of -1.5 , the increase in sensitivity of the Lockman Hole radio map compared to that of the ECDF-S produces a density of sources that is higher by almost a factor of 2 at the parts of the map corresponding to that sensitivity. However, we also note that the radio map of the Subaru *XMM-Newton* Deep Field (SXDF) that was used to find counterparts to that portion of SHADES had a similar depth to the ECDF-S map ($6.3 \mu\text{Jy beam}^{-1}$), but produced a significantly greater fraction of SMGs with robust IDs, 58 per cent (Ivison et al. 2007).

We now go on to consider other reasons why true counterparts might be missed, beginning by noting that a small number (≈ 5) of the SMG detections are likely to be spurious (Weiß et al. 2009), as is common in surveys of this kind. Other possible reasons include:

- (i) the counterpart lies outside the search radius and
- (ii) multiple SMGs have become blended due to the low resolution of the submm data.

Table 2. 24- μm properties of potential counterparts to LESS 870- μm sources in the ECDF-S. SMGs are listed in order of decreasing S/N. Those SMG names that are appended with an ‘*’ are not fully covered by the FIDEL map. Secure counterparts ($p \leq 0.05$) are in boldface and where p lies between 0.05 and 1.0 this is given in parentheses. Counterparts where $0.05 < p \leq 0.1$ is obtained at two out of radio (Table 2), 24 or 5.8- μm (Table 3) have their value of p given in boldface within parentheses.

ID	SMG name	Submm position		r_s (arcsec)	24- μm position		24- μm flux (μJy)	Offset (arcsec)	p
		(α_{J2000})	(δ_{J2000})		(α_{J2000})	(δ_{J2000})			
001	LESS J033314.3–275611	03:33:14.26	–27:56:11.2	3.1	03:33:14.4124	–27:56:11.995	38.0 ± 7.9	2.2	0.053
002	LESS J033302.5–275643	03:33:02.50	–27:56:43.6	3.8	03:33:02.5305	–27:56:45.344	186.5 ± 22.6	1.8	0.014
003	LESS J033321.5–275520	03:33:21.51	–27:55:20.2	3.8	03:33:21.5113	–27:55:20.515	33.6 ± 7.4	0.3	0.004
004	LESS J033136.0–275439	03:31:36.01	–27:54:39.2	4.1	–	–	–	–	–
005	LESS J033129.5–275907	03:31:29.46	–27:59:07.3	4.6	–	–	–	–	–
006	LESS J033257.1–280102	03:32:57.14	–28:01:02.1	4.8	03:32:57.0774	–28:01:01.074	35.7 ± 9.6	1.3	0.041
007	LESS J033315.6–274523	03:33:15.55	–27:45:23.6	5.1	03:33:15.3999	–27:45:24.008	368.3 ± 8.1	2.0	0.008
008	LESS J033205.1–273108	03:32:05.07	–27:31:08.8	4.0	–	–	–	–	–
009	LESS J033211.3–275210	03:32:11.29	–27:52:10.4	5.1	03:32:11.3060	–27:52:13.235	110.6 ± 10.6	2.8	(0.063)
010	LESS J033219.0–275219	03:32:19.02	–27:52:19.4	5.1	03:32:19.0566	–27:52:14.801	119.8 ± 18.0	4.6	(0.090)
011	LESS J033213.6–275602	03:32:13.58	–27:56:02.5	5.2	03:32:13.8449	–27:55:59.965	103.1 ± 8.4	4.3	0.113
012	LESS J033248.1–275414	03:32:48.12	–27:54:14.7	5.3	03:32:47.7383	–27:54:13.569	33.7 ± 9.3	5.2	0.178
					03:32:48.0689	–27:54:16.266	43.2 ± 8.8	1.7	(0.058)
					03:32:48.5059	–27:54:15.795	174.3 ± 9.5	5.2	(0.095)
013	LESS J033249.2–274246	03:32:49.23	–27:42:46.6	5.3	–	–	–	–	–
014	LESS J033152.6–280320	03:31:52.64	–28:03:20.4	5.1	03:31:52.4265	–28:03:18.033	95.5 ± 9.5	3.7	(0.096)
015	LESS J033333.4–275930	03:33:33.36	–27:59:30.1	5.3	03:33:33.3439	–27:59:29.407	108.6 ± 10.1	0.7	0.008
016	LESS J033218.9–273738	03:32:18.89	–27:37:38.7	5.8	–	–	–	–	–
017	LESS J033207.6–275123	03:32:07.59	–27:51:23.0	6.1	03:32:07.2947	–27:51:20.431	219.3 ± 7.7	4.7	(0.071)
018	LESS J033205.1–274652	03:32:05.12	–27:46:52.1	6.2	03:32:05.0405	–27:46:55.728	39.9 ± 6.6	3.8	0.174
					03:32:04.8558	–27:46:47.248	560.5 ± 8.2	6.0	0.029
019	LESS J033208.1–275818	03:32:08.10	–27:58:18.7	6.4	03:32:07.8975	–27:58:23.595	40.0 ± 8.6	5.6	0.239
					03:32:08.2306	–27:58:14.218	79.8 ± 7.5	4.8	0.172
					03:33:16.7545	–28:00:15.608	176.6 ± 7.6	4.1	(0.078)
020	LESS J033316.6–280018	03:33:16.56	–28:00:18.8	6.5	03:33:16.7545	–28:00:15.608	176.6 ± 7.6	4.1	(0.078)
021	LESS J033329.9–273441	03:33:29.93	–27:34:41.7	6.2	03:33:29.7579	–27:34:46.266	217.1 ± 21.8	5.1	(0.067)
022	LESS J033147.0–273243	03:31:47.02	–27:32:43.0	5.9	03:31:46.9134	–27:32:38.841	409.8 ± 12.7	4.4	0.025
023	LESS J033212.1–280508	03:32:12.11	–28:05:08.5	5.8	03:32:11.9457	–28:05:06.229	35.7 ± 10.2	3.1	0.135
024	LESS J033336.8–274401	03:33:36.79	–27:44:01.0	6.3	03:33:36.9853	–27:43:58.522	130.2 ± 9.3	3.6	(0.086)
025	LESS J033157.1–275940	03:31:57.05	–27:59:40.8	6.8	03:31:56.8419	–27:59:38.856	233.2 ± 8.0	3.4	0.043
026	LESS J033136.9–275456	03:31:36.90	–27:54:56.1	7.0	–	–	–	–	–
027	LESS J033149.7–273432	03:31:49.73	–27:34:32.7	6.5	03:31:49.8900	–27:34:36.658	171.9 ± 16.4	4.5	(0.082)
					03:31:50.2090	–27:34:32.901	277.3 ± 18.8	6.4	(0.072)
028	LESS J033302.9–274432	03:33:02.92	–27:44:32.6	6.9	–	–	–	–	–
029	LESS J033336.9–275813	03:33:36.90	–27:58:13.0	6.6	03:33:36.8692	–27:58:08.874	136.0 ± 9.2	4.1	(0.103)
030	LESS J033344.4–280346	03:33:44.37	–28:03:46.1	5.5	–	–	–	–	–
031	LESS J033150.0–275743	03:31:49.96	–27:57:43.9	7.2	03:31:49.7330	–27:57:39.858	66.2 ± 9.0	5.0	0.214
032	LESS J033243.6–274644	03:32:43.57	–27:46:44.0	7.2	03:32:43.5139	–27:46:39.630	81.5 ± 13.4	4.4	0.157
033	LESS J033149.8–275332	03:31:49.78	–27:53:32.9	7.2	–	–	–	–	–
034	LESS J033217.6–275230	03:32:17.64	–27:52:30.3	7.2	03:32:17.5943	–27:52:28.656	223.3 ± 9.4	1.8	0.016
035	LESS J033110.3–273714	03:31:10.35	–27:37:14.8	5.9	03:31:10.4778	–27:37:15.134	73.3 ± 9.6	1.7	0.046
036	LESS J033149.2–280208	03:31:49.15	–28:02:08.7	7.2	03:31:48.9432	–28:02:13.486	274.5 ± 9.6	5.5	(0.071 + radio)
037	LESS J033336.0–275347	03:33:36.04	–27:53:47.6	6.9	03:33:36.0581	–27:53:49.812	201.8 ± 19.7	2.2	0.025
					03:33:36.2881	–27:53:47.112	92.4 ± 19.4	3.3	(0.092)
038	LESS J033310.2–275641	03:33:10.20	–27:56:41.5	7.5	03:33:10.0986	–27:56:45.026	154.9 ± 6.8	3.8	(0.086)
					03:33:10.5182	–27:56:44.627	78.4 ± 7.5	5.2	0.216
039	LESS J033144.9–273435	03:31:44.90	–27:34:35.4	7.3	03:31:45.0100	–27:34:36.567	131.0 ± 7.5	1.9	0.036
040	LESS J033246.7–275120	03:32:46.74	–27:51:20.9	7.6	03:32:46.8016	–27:51:20.648	119.8 ± 7.2	0.9	0.011
041	LESS J033110.5–275233	03:31:10.47	–27:52:33.2	6.2	–	–	–	–	–
042	LESS J033231.0–275858	03:32:31.02	–27:58:58.1	7.7	03:32:30.9901	–27:59:02.928	70.5 ± 17.5	4.8	0.180
043	LESS J033307.0–274801	03:33:07.00	–27:48:01.0	7.6	03:33:06.6209	–27:48:02.051	229.6 ± 7.2	5.1	(0.086)
					03:33:07.4686	–27:47:59.241	190.1 ± 10.8	6.5	0.140
					03:33:07.1581	–27:47:55.911	77.7 ± 9.9	5.5	0.224
044	LESS J033131.0–273238	03:31:30.96	–27:32:38.5	6.9	03:31:31.2040	–27:32:38.469	400.9 ± 13.0	3.2	0.017
045	LESS J033225.7–275228	03:32:25.71	–27:52:28.5	7.7	03:32:25.2320	–27:52:30.520	116.1 ± 8.1	6.7	0.226
046	LESS J033336.8–273247*	03:33:36.80	–27:32:47.0	6.5	–	–	–	–	–
047	LESS J033256.0–273317	03:32:56.00	–27:33:17.7	7.2	03:32:55.9048	–27:33:19.557	55.9 ± 9.7	2.2	(0.089)
048	LESS J033237.8–273202	03:32:37.77	–27:32:02.0	6.8	03:32:37.9882	–27:31:59.611	406.8 ± 11.9	3.8	0.021
049	LESS J033124.4–275040	03:31:24.45	–27:50:40.9	7.6	03:31:24.4752	–27:50:37.619	113.5 ± 14.6	3.3	(0.090)
					03:31:24.7116	–27:50:46.277	122.9 ± 11.6	6.4	0.198
					03:31:24.2346	–27:50:43.663	120.3 ± 9.3	4.0	0.118

Table 2 – continued

ID	SMG name	Submm position		r_s (arcsec)	24- μ m position		24- μ m flux (μ Jy)	Offset (arcsec)	p
		(α_{J2000})	(δ_{J2000})		(α_{J2000})	(δ_{J2000})			
050	LESS J033141.2–274441	03:31:41.15	–27:44:41.5	7.9	03:31:41.3603	–27:44:47.005	197.4 \pm 12.5	6.2	0.127
					03:31:41.1223	–27:44:42.531	64.4 \pm 12.3	1.1	0.028
					03:31:41.5587	–27:44:40.948	101.9 \pm 10.2	5.5	0.196
					03:31:40.6007	–27:44:40.929	175.0 \pm 9.5	7.3	0.183
					03:31:40.9980	–27:44:34.928	306.6 \pm 24.1	6.9	(0.072)
051	LESS J033144.8–274425	03:31:44.81	–27:44:25.1	7.9	03:31:45.0279	–27:44:27.859	117.1 \pm 8.5	4.0	0.125
					03:31:44.4130	–27:44:20.236	93.0 \pm 9.6	7.2	0.271
052	LESS J033128.5–275601	03:31:28.51	–27:56:01.3	7.9	03:31:28.3837	–27:56:07.987	127.8 \pm 14.0	6.9	0.203
053	LESS J033159.1–275435	03:31:59.12	–27:54:35.5	8.0	03:31:58.9803	–27:54:38.097	137.5 \pm 8.3	3.2	(0.079)
054	LESS J033243.6–273353	03:32:43.61	–27:33:53.6	7.6	03:32:43.6418	–27:33:56.925	222.1 \pm 8.8	3.4	0.048
055	LESS J033302.2–274033	03:33:02.20	–27:40:33.6	8.0	–	–	–	–	–
056	LESS J033153.2–273936	03:31:53.17	–27:39:36.1	8.1	03:31:53.1272	–27:39:37.490	270.3 \pm 11.4	1.5	0.010
057	LESS J033152.0–275329	03:31:51.97	–27:53:29.7	8.0	03:31:51.9121	–27:53:26.733	297.2 \pm 8.4	3.1	0.027
058	LESS J033225.8–273306	03:32:25.79	–27:33:06.7	7.6	–	–	–	–	–
059	LESS J033303.9–274412	03:33:03.87	–27:44:12.2	8.2	03:33:03.6615	–27:44:11.811	172.1 \pm 10.6	2.8	0.050
060	LESS J033317.5–275121	03:33:17.47	–27:51:21.5	8.3	03:33:17.4868	–27:51:28.081	292.8 \pm 9.8	6.6	(0.089 + radio)
061	LESS J033245.6–280025	03:32:45.63	–28:00:25.3	8.3	03:32:45.9477	–28:00:22.155	58.6 \pm 7.9	5.3	0.264
062	LESS J033236.4–273452	03:32:36.41	–27:34:52.5	8.2	03:32:36.5400	–27:34:53.319	243.5 \pm 35.6	1.9	0.014
					03:32:36.1180	–27:34:53.299	65.1 \pm 14.6	4.0	0.167
063	LESS J033308.5–280044	03:33:08.46	–28:00:44.3	8.3	03:33:08.4096	–28:00:42.440	62.4 \pm 9.8	2.0	(0.073)
064	LESS J033201.0–280025	03:32:01.00	–28:00:25.6	8.4	03:32:00.5600	–28:00:25.733	83.1 \pm 17.1	5.8	0.215
					03:32:00.9399	–28:00:25.316	338.4 \pm 17.2	0.8	0.002
065	LESS J033252.4–273527	03:32:52.40	–27:35:27.7	8.3	–	–	–	–	–
066	LESS J033331.7–275406	03:33:31.69	–27:54:06.1	8.2	03:33:31.9057	–27:54:10.024	543.7 \pm 12.3	4.9	0.023
067	LESS J033243.3–275517	03:32:43.28	–27:55:17.9	8.4	03:32:43.7519	–27:55:16.397	109.6 \pm 6.4	6.4	0.240
					03:32:43.0426	–27:55:24.757	209.4 \pm 7.1	7.5	0.167
					03:32:43.1879	–27:55:14.295	516.4 \pm 8.0	3.8	0.017
068	LESS J033233.4–273918	03:32:33.44	–27:39:18.5	8.4	03:32:33.3296	–27:39:13.479	41.9 \pm 9.4	5.2	0.291
					03:32:33.9234	–27:39:14.713	191.7 \pm 8.2	7.5	0.180
069	LESS J033134.3–275934	03:31:34.26	–27:59:34.3	8.5	03:31:33.8107	–27:59:32.287	97.0 \pm 11.7	6.3	0.241
					03:31:34.6801	–27:59:34.629	134.1 \pm 17.2	5.6	0.155
070	LESS J033144.0–273832	03:31:43.97	–27:38:32.5	8.5	03:31:44.0299	–27:38:35.076	365.2 \pm 17.4	2.7	0.015
					03:31:43.9688	–27:38:30.430	85.5 \pm 18.7	2.1	(0.058)
071	LESS J033306.3–273327	03:33:06.29	–27:33:27.7	8.0	–	–	–	–	–
072	LESS J033240.4–273802	03:32:40.40	–27:38:02.5	8.5	03:32:40.0462	–27:38:08.479	471.4 \pm 22.9	7.6	0.051
073	LESS J033229.3–275619	03:32:29.33	–27:56:19.3	8.5	–	–	–	–	–
074	LESS J033309.3–274809	03:33:09.34	–27:48:09.9	8.4	03:33:09.1309	–27:48:16.747	202.0 \pm 23.4	7.4	0.135
					03:33:09.3973	–27:48:14.431	55.4 \pm 9.5	4.6	0.234
					03:33:09.5602	–27:48:03.494	291.2 \pm 25.0	7.0	(0.082)
					03:33:09.0479	–27:48:07.069	37.1 \pm 9.1	4.8	0.278
075	LESS J033126.8–275554	03:31:26.83	–27:55:54.6	8.4	03:31:27.1769	–27:55:50.848	1018.1 \pm 38.3	5.9	0.011
076	LESS J033332.7–275957	03:33:32.67	–27:59:57.2	8.4	–	–	–	–	–
077	LESS J033157.2–275633	03:31:57.23	–27:56:33.2	8.8	03:31:56.7468	–27:56:37.786	48.0 \pm 10.2	7.9	0.382
					03:31:56.8109	–27:56:32.398	32.3 \pm 8.9	5.6	0.339
					03:31:57.2381	–27:56:40.234	149.6 \pm 7.9	7.0	0.217
					03:31:57.6947	–27:56:28.842	129.8 \pm 6.7	7.5	0.261
078	LESS J033340.3–273956*	03:33:40.30	–27:39:56.9	8.4	–	–	–	–	–
079	LESS J033221.2–275623	03:32:21.25	–27:56:23.5	8.8	03:32:21.5939	–27:56:23.782	520.7 \pm 9.2	4.6	0.023
					03:32:21.1259	–27:56:26.704	64.8 \pm 7.3	3.6	0.171
					03:32:20.8843	–27:56:18.455	42.5 \pm 6.7	7.0	0.381
					03:32:21.4284	–27:56:16.710	140.5 \pm 7.9	7.2	0.234
080	LESS J033142.2–274834	03:31:42.23	–27:48:34.4	8.9	03:31:42.6032	–27:48:41.050	138.2 \pm 8.1	8.3	0.277
					03:31:42.7846	–27:48:36.479	79.8 \pm 5.8	7.6	0.344
081	LESS J033127.4–274440	03:31:27.45	–27:44:40.4	8.8	03:31:27.5539	–27:44:39.264	523.6 \pm 11.0	1.8	0.005
082	LESS J033253.8–273810	03:32:53.77	–27:38:10.9	9.0	03:32:53.5601	–27:38:14.872	64.4 \pm 10.3	4.9	0.241
083	LESS J033308.9–280522	03:33:08.92	–28:05:22.0	8.3	03:33:08.8774	–28:05:14.298	59.5 \pm 8.8	7.7	0.352
084	LESS J033154.2–275109	03:31:54.22	–27:51:09.8	8.9	03:31:54.8059	–27:51:10.132	98.7 \pm 7.6	7.8	0.318
					03:31:54.5080	–27:51:05.155	133.5 \pm 7.3	6.0	0.200
					03:31:53.8175	–27:51:03.834	141.6 \pm 7.6	8.0	0.263
085	LESS J033110.3–274503	03:31:10.28	–27:45:03.1	7.7	–	–	–	–	–
086	LESS J033114.9–274844	03:31:14.90	–27:48:44.3	8.5	–	–	–	–	–
087	LESS J033251.1–273143	03:32:51.09	–27:31:43.0	8.4	03:32:51.6586	–27:31:40.858	55.8 \pm 10.6	7.9	0.349
					03:32:50.8267	–27:31:41.290	419.4 \pm 13.2	3.9	0.023

Table 2 – *continued*

ID	SMG name	Submm position (α_{J2000} δ_{J2000})		r_s (arcsec)	24- μm position (α_{J2000} δ_{J2000})		24- μm flux (μJy)	Offset (arcsec)	p
088	LESS J033155.2–275345	03:31:55.19	–27:53:45.3	9.0	03:31:55.7552	–27:53:47.714	195.4 \pm 7.2	7.9	0.197
089	LESS J033248.4–280023	03:32:48.44	–28:00:23.8	9.1	03:31:54.7914	–27:53:41.259	269.5 \pm 19.4	6.7	(0.094)
090	LESS J033243.7–273554	03:32:43.65	–27:35:54.1	9.1	–	–	–	–	–
091	LESS J033135.2–274033	03:31:35.25	–27:40:33.7	9.1	03:31:35.0211	–27:40:38.070	44.8 \pm 9.5	5.3	0.309
092	LESS J033138.4–274336	03:31:38.36	–27:43:36.0	9.2	03:31:38.2703	–27:43:39.387	101.3 \pm 9.2	3.6	0.130
093	LESS J033110.8–275607	03:31:10.84	–27:56:07.2	8.4	03:31:38.2101	–27:43:28.525	66.7 \pm 13.5	7.7	0.342
094	LESS J033307.3–275805	03:33:07.27	–27:58:05.0	9.1	–	–	–	–	–
095	LESS J033241.7–275846	03:32:41.74	–27:58:46.1	9.2	03:33:07.6169	–27:58:06.076	106.2 \pm 7.3	4.7	0.180
096	LESS J033313.0–275556	03:33:13.03	–27:55:56.8	9.2	03:33:06.6787	–27:58:06.259	70.6 \pm 6.7	7.9	0.376
097	LESS J033313.7–273803	03:33:13.65	–27:38:03.4	9.2	03:32:41.2420	–27:58:41.239	328.8 \pm 6.5	8.2	0.110
098	LESS J033130.2–275726	03:31:30.22	–27:57:26.0	9.3	03:33:12.6193	–27:55:51.500	961.6 \pm 9.0	7.6	0.023
099	LESS J033251.4–275536	03:32:51.45	–27:55:36.0	9.2	03:33:13.0725	–27:55:55.873	33.1 \pm 7.6	1.1	0.042
100	LESS J033111.3–280006	03:31:11.32	–28:00:06.2	8.8	–	–	–	–	–
101	LESS J033151.5–274552	03:31:51.47	–27:45:52.1	9.3	03:31:29.9230	–27:57:22.432	268.8 \pm 15.7	5.3	(0.073)
102	LESS J033335.6–274020	03:33:35.61	–27:40:20.1	9.2	03:32:51.3366	–27:55:43.489	120.9 \pm 6.2	7.6	0.287
103	LESS J033325.3–273400	03:33:25.35	–27:34:00.4	9.2	–	–	–	–	–
104	LESS J033258.5–273803	03:32:58.46	–27:38:03.0	9.4	03:31:51.3802	–27:46:00.784	43.9 \pm 6.6	8.8	0.448
105	LESS J033115.8–275313	03:31:15.78	–27:53:13.1	9.0	03:33:35.5719	–27:40:22.963	318.4 \pm 16.5	2.9	0.022
106	LESS J033140.1–275631	03:31:40.09	–27:56:31.4	9.4	03:33:25.3661	–27:33:58.314	113.3 \pm 13.5	2.1	0.052
107	LESS J033130.8–275150	03:31:30.85	–27:51:50.9	9.4	03:32:57.8377	–27:37:59.368	108.2 \pm 10.0	9.0	0.354
108	LESS J033316.4–275033	03:33:16.42	–27:50:33.1	9.5	03:31:40.4427	–27:56:34.335	65.7 \pm 10.2	5.5	0.282
109	LESS J033328.1–274157	03:33:28.08	–27:41:57.0	9.5	03:31:40.1806	–27:56:22.325	363.6 \pm 10.2	9.2	0.113
110	LESS J033122.6–275417	03:31:22.64	–27:54:17.2	9.4	03:31:31.3083	–27:51:53.866	89.4 \pm 9.6	6.8	0.301
111	LESS J033325.6–273423	03:33:25.58	–27:34:23.0	9.4	03:31:30.5400	–27:51:58.629	96.9 \pm 9.4	8.8	0.365
112	LESS J033249.3–273112	03:32:49.28	–27:31:12.3	9.0	03:31:30.6286	–27:51:45.285	124.2 \pm 16.5	6.3	0.208
113	LESS J033236.4–275845	03:32:36.42	–27:58:45.9	9.5	03:31:31.2827	–27:51:43.895	321.7 \pm 9.2	9.1	0.131
114	LESS J033150.8–274438	03:31:50.81	–27:44:38.5	9.7	03:31:30.3348	–27:51:48.424	102.8 \pm 10.9	7.3	0.295
115	LESS J033349.7–274239*	03:33:49.71	–27:42:39.2	8.9	03:33:16.4864	–27:50:39.550	3722.6 \pm 73.7	6.5	0.002
116	LESS J033154.4–274525	03:31:54.42	–27:45:25.5	9.7	03:33:27.9952	–27:42:02.797	169.0 \pm 15.5	5.9	0.151
117	LESS J033128.0–273925	03:31:28.02	–27:39:25.2	9.7	03:33:28.5385	–27:41:51.142	128.8 \pm 13.3	8.4	0.289
118	LESS J033121.8–274936	03:31:21.81	–27:49:36.8	9.7	03:31:22.6458	–27:54:21.881	104.3 \pm 16.6	4.7	0.165
119	LESS J033256.5–280319	03:32:56.51	–28:03:19.1	9.7	03:33:25.2095	–27:34:23.302	353.7 \pm 53.3	4.9	0.031
120	LESS J033328.4–275655	03:33:28.45	–27:56:55.9	9.8	03:32:48.8281	–27:31:12.959	190.8 \pm 13.2	6.0	0.136
121	LESS J033333.3–273449*	03:33:33.32	–27:34:49.3	9.7	03:31:50.7294	–27:44:40.607	73.6 \pm 18.5	2.4	(0.083)
122	LESS J033139.6–274120	03:31:39.62	–27:41:20.4	9.9	03:31:51.0920	–27:44:37.132	515.0 \pm 7.8	4.0	0.019
123	LESS J033330.9–275349	03:33:30.88	–27:53:49.3	9.8	03:31:50.9679	–27:44:43.872	59.8 \pm 6.5	5.8	0.320
124	LESS J033203.6–273605	03:32:03.59	–27:36:05.0	10.0	–	–	–	–	–
125	LESS J033146.0–274621	03:31:46.02	–27:46:21.2	9.9	03:31:27.5895	–27:39:27.598	203.1 \pm 13.1	6.2	0.137
126	LESS J033209.8–274102	03:32:09.76	–27:41:02.0	9.9	03:31:21.7699	–27:49:41.451	53.8 \pm 8.6	4.7	0.269
					03:32:56.5806	–28:03:11.789	168.6 \pm 7.0	7.4	0.219
					03:33:29.0593	–27:56:57.375	47.8 \pm 9.6	8.2	0.442
					03:33:28.5322	–27:56:54.295	345.6 \pm 9.5	1.9	0.010
					–	–	–	–	–
					03:31:39.5353	–27:41:19.449	1392.5 \pm 15.8	1.5	0.001
					–	–	–	–	–
					03:32:03.8787	–27:36:06.030	123.4 \pm 10.6	4.0	0.131
					03:32:03.0844	–27:36:01.864	71.2 \pm 10.0	7.4	0.375
					03:31:46.3415	–27:46:23.329	36.4 \pm 7.1	4.8	0.316
					03:31:45.5405	–27:46:15.445	50.7 \pm 8.6	8.6	0.462
					03:32:09.5687	–27:41:06.810	263.4 \pm 8.7	5.4	(0.086)
					03:32:10.1562	–27:40:56.226	44.3 \pm 8.0	7.8	0.451

6.1 Search radius and radio astrometry

As it is necessary to impose a limit to how far you search from an SMG position, and because choosing too large a radius increases the chances of finding unrelated counterparts whilst reducing the significance of genuine associations – it is likely that a small num-

ber of SMGs will not have been searched out to a sufficient radius to locate their counterpart. We have estimated that this will amount to 1–2 counterparts, but if we have underestimated the size of the submm positional errors then this number will be larger. Taking SHADES as an example, Ivison et al. (2007) estimated that 5 per cent of counterparts would be missed in this manner and recent

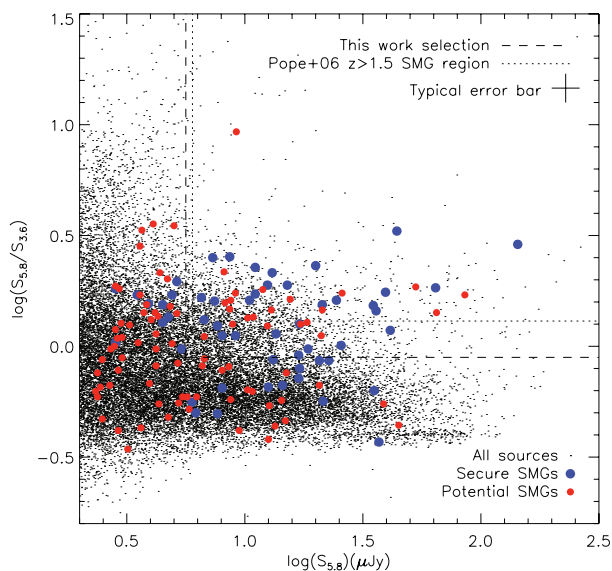


Figure 3. 3.6- and 5.8- μm colour-flux diagram for IRAC-selected sources in the ECDF-S. Secure radio- and MIPS-identified SMG counterparts, and potential SMG counterparts are highlighted. The secure radio- and MIPS-identified SMG counterparts are typically redder than the field population, a property which we use to define the marked selection criteria for SMGs (dashed rectangle). Within this region there is a 10 per cent contamination rate from field galaxies, and we recover 78 per cent of the secure radio- and MIPS-identified SMG counterparts. The dotted rectangle shows the region defined by Pope et al. (2006).

Submillimeter Array (SMA) observations with subarcsec accuracy have identified one example of this, SXDF850.06 lying just outside the Ivison et al. (2007) 8-arcsec search radius (Hatsukade et al. 2010).

Errors in the absolute astrometric accuracy of the MIPS and radio catalogues will also affect our ability to reliably determine counterparts. In Fig. 4 we show the differences between the right ascension and declination for each counterpart that has emission at both 24 μm and 21 cm. There is a clear offset between the two which has a median value of -0.25 arcsec in right ascension and $+0.39$ arcsec in declination (MIPS – radio). In order to improve the determination of this offset, we have used TOPCAT (Taylor 2005) to measure the median offset between the radio and MIPS catalogues by finding all unique matches within 2 arcsec. These 2019 matches are also plotted in Fig. 4 and have similar median offsets of -0.25 arcsec in right ascension and $+0.29$ arcsec in declination.

Applying these more accurate offsets during the p -statistic procedure as if they purely originated from the MIPS data reduces the number of robust counterparts by one, whereas assuming that the origin lies with the radio data increases the number of robust counterparts by one. Hence, the effect of the offsets is actually rather small and the additional radio counterpart is found anyway without the offsets applied due to it having $p < 0.1$ in both the MIPS and radio. As a result, we have not taken the offsets into account when calculating the values of p and the radio positions given in Table 1 have not been corrected for them.

As a test of our search radius strategy, we have examined the distribution of the radial offsets between the radio and 24- μm secure counterparts and their SMG. If these truly originate from random uncertainties in the positions of the SMGs, then they should conform to a Rayleigh distribution. In addition, we note that this should only be the case if the offsets are calculated as a multiple of the 1σ

SMG position uncertainty. Fig. 5 shows the positional offsets for both the radio and MIPS data in bins of 0.5σ , with a fitted Rayleigh distribution overplotted. Writing this as $R(r) \propto r e^{-r^2/2\rho^2}$, the width parameter ρ is equal to the one-dimensional standard deviation of the positional errors. As we are plotting these in units of standard deviations, then by definition this parameter (which is also equal to the mode of the distribution) should be equal to unity.

In the case of the MIPS data, the fit to the data is excellent with a reduced chi-square of 0.7 and a value for the width parameter, ρ , of 0.91 ± 0.08 . This strongly suggests that we have correctly calculated the magnitude of the positional errors and that our assumption that the offsets originate predominantly in the submm source position is also correct. The fit in the case of the radio data is formally very similar, but has a larger value of $\rho = 1.30 \pm 0.13$, a 2.3σ deviation from the expected value of 1.0. Given that the 24- μm data give the expected answer, this points to something special about the radio positional offsets, separate from the astrometric error already identified (which has been removed when calculating the offsets displayed in Fig. 5). If the larger offset in the radio is not a statistical fluke, then it points to an additional, systematic offset between the radio and the MIPS/submm position, perhaps due to emission from more extended or structured radio emission e.g. radio jets.

6.2 Blending of SMGs

The second potential cause of the low identification rate is that the SMG, instead of being a single unresolved source, may actually be a blend of several sources. This is more likely to be the case here than many other submm surveys due to the slightly larger beam size, 19 arcsec compared to the 14 arcsec of the JCMT/SCUBA and the 11 arcsec of the IRAM 30-m/MAMBO (we note, however, that the lack of chopping for LABOCA reduces the possibility of confusion from that source in these maps). The problem is that the p -statistic implicitly assumes that the submm position corresponds to a single source; if multiple sources are responsible for the submm emission, the SMG centroid will be offset from the genuine counterparts which are less likely to fall within the search radius.

A visual inspection of the plots in Fig. A1 makes it clear that this is often the case. One noteworthy case is the chain of three MIPS galaxies visible under LESS004. This source is clearly elongated along the axis of the galaxy chain and as two of the galaxies are detected in the radio map they presumably both contribute to the submm emission. As the resolution of the submm map is not sufficient to separate the individual sources, it has instead been classified as a single source with its centroid lying in between the two radio sources. This places it close, but not close enough, to the third galaxy which is also radio quiet. We further note that this chain of galaxies continues to the south where it blends into another submm source, LESS026.

The use of an S/N-dependent search radius makes it more likely that sources that are blended are not robustly identified as the summed submm flux density causes a smaller value of r_s to be used than if a constant radius were adopted. This alternative approach often chooses a search radius that is large enough to maximize the probability of detecting counterparts to the weaker SMGs (of which the median submm flux density is often representative) that have larger positional errors. However, the cost of this is that higher values of p are measured for unblended, brighter SMGs which results in potentially less counterparts being identified.

Finally, in forming the p -statistic, we have only included radio and MIPS sources with $S/N \geq 3.5$ (the IRAC sources were all much more significantly detected due to all sources being brighter than

Table 3. IRAC properties of potential counterparts to LESS 870- μm sources in the ECDF-S that do not have robust counterparts identified in either the radio or at 24 μm and fall within the colour-flux cut shown in Fig. 3. SMGs are listed in order of decreasing S/N. Secure counterparts ($p \leq 0.05$) are in boldface and where p lies between 0.05 and 0.1 this is given in parentheses. One counterpart where $0.05 < p \leq 0.1$ is also obtained in the radio (Tables 1 and 2) is also considered robust and has its value of p given in boldface within parentheses. Those SMG names that are appended with an ‘**’ are not fully covered by the SIMPLE data at both 3.6- and 5.8- μm and so counterparts for them could not be found with this method.

ID	SMG name	Submm position		r_s (arcsec)	5.8- μm position		5.8- μm flux (μJy)	Offset (arcsec)	p
		(α_{J2000})	(δ_{J2000})		(α_{J2000})	(δ_{J2000})			
004	LESS J033136.0–275439	03:31:36.01	–27:54:39.2	4.1	–	–	–	–	–
005	LESS J033129.5–275907	03:31:29.46	–27:59:07.3	4.6	–	–	–	–	–
008	LESS J033205.1–273108	03:32:05.07	–27:31:08.8	4.0	–	–	–	–	–
013	LESS J033249.2–274246	03:32:49.23	–27:42:46.6	5.3	–	–	–	–	–
019	LESS J033208.1–275818	03:32:08.10	–27:58:18.7	6.4	03:32:07.9138	–27:58:23.279	6.7 ± 1.2	5.2	0.053
					03:32:08.2382	–27:58:13.717	6.7 ± 1.2	5.3	0.053
021	LESS J033329.9–273441	03:33:29.93	–27:34:41.7	6.2	–	–	–	–	–
023	LESS J033212.1–280508	03:32:12.11	–28:05:08.5	5.8	–	–	–	–	–
026	LESS J033136.9–275456	03:31:36.90	–27:54:56.1	7.0	–	–	–	–	–
027	LESS J033149.7–273432	03:31:49.73	–27:34:32.7	6.5	03:31:49.9238	–27:34:36.790	9.6 ± 1.5	4.8	0.040
					03:31:49.8854	–27:34:30.428	6.1 ± 1.2	3.1	0.033
028	LESS J033302.9–274432	03:33:02.92	–27:44:32.6	6.9	–	–	–	–	–
030	LESS J033344.4–280346	03:33:44.37	–28:03:46.1	5.5	–	–	–	–	–
031	LESS J033150.0–275743	03:31:49.96	–27:57:43.9	7.2	03:31:49.7364	–27:57:39.280	7.4 ± 1.3	5.5	(0.059)
					03:31:49.7741	–27:57:40.439	7.7 ± 1.3	4.2	0.044
032	LESS J033243.6–274644	03:32:43.57	–27:46:44.0	7.2	03:32:43.5170	–27:46:38.978	6.5 ± 1.2	5.1	(0.059)
033	LESS J033149.8–275332	03:31:49.78	–27:53:32.9	7.2	–	–	–	–	–
038	LESS J033310.2–275641	03:33:10.20	–27:56:41.5	7.5	–	–	–	–	–
041	LESS J033110.5–275233	03:31:10.47	–27:52:33.2	6.2	03:31:10.0942	–27:52:36.347	39.6 ± 3.1	5.9	0.010
042	LESS J033231.0–275858	03:32:31.02	–27:58:58.1	7.7	–	–	–	–	–
043	LESS J033307.0–274801	03:33:07.00	–27:48:01.0	7.6	03:33:07.4822	–27:47:59.172	9.2 ± 1.4	6.7	(0.065)
					03:33:06.6365	–27:48:01.919	13.3 ± 1.7	4.9	0.035
045	LESS J033225.7–275228	03:32:25.71	–27:52:28.5	7.7	03:32:25.2458	–27:52:30.162	15.1 ± 1.8	6.4	0.042
047	LESS J033256.0–273317	03:32:56.00	–27:33:17.7	7.2	03:32:55.9356	–27:33:19.678	7.3 ± 1.3	2.2	0.019
					03:32:55.9910	–27:33:18.900	6.9 ± 1.2	1.2	0.008
051	LESS J033144.8–274425	03:31:44.81	–27:44:25.1	7.9	–	–	–	–	–
052	LESS J033128.5–275601	03:31:28.51	–27:56:01.3	7.9	–	–	–	–	–
053	LESS J033159.1–275435	03:31:59.12	–27:54:35.5	8.0	–	–	–	–	–
055	LESS J033302.2–274033	03:33:02.20	–27:40:33.6	8.0	–	–	–	–	–
058	LESS J033225.8–273306	03:32:25.79	–27:33:06.7	7.6	–	–	–	–	–
061	LESS J033245.6–280025	03:32:45.63	–28:00:25.3	8.3	–	–	–	–	–
065	LESS J033252.4–273527	03:32:52.40	–27:35:27.7	8.3	–	–	–	–	–
068	LESS J033233.4–273918	03:32:33.44	–27:39:18.5	8.4	–	–	–	–	–
069	LESS J033134.3–275934	03:31:34.26	–27:59:34.3	8.5	03:31:33.7745	–27:59:32.150	13.0 ± 1.7	6.8	(0.057)
					03:31:34.6841	–27:59:33.029	7.3 ± 1.3	5.8	(0.074)
071	LESS J033306.3–273327	03:33:06.29	–27:33:27.7	8.0	–	–	–	–	–
074	LESS J033309.3–274809	03:33:09.34	–27:48:09.9	8.4	03:33:09.1416	–27:48:16.650	14.0 ± 1.7	7.2	(0.057 + radio)
					03:33:09.3454	–27:48:15.998	12.6 ± 1.7	6.1	0.051
077	LESS J033157.2–275633	03:31:57.23	–27:56:33.2	8.8	03:31:57.2544	–27:56:39.815	11.6 ± 1.6	6.6	(0.062)
080	LESS J033142.2–274834	03:31:42.23	–27:48:34.4	8.9	03:31:42.5995	–27:48:41.155	8.0 ± 1.3	8.3	0.101
					03:31:42.8066	–27:48:36.659	11.9 ± 1.6	8.0	(0.076)
					03:31:41.6700	–27:48:30.031	10.4 ± 1.5	8.6	(0.090)
					03:32:53.9789	–27:38:14.633	5.7 ± 1.1	4.7	(0.072)
082	LESS J033253.8–273810	03:32:53.77	–27:38:10.9	9.0	–	–	–	–	–
083	LESS J033308.9–280522	03:33:08.92	–28:05:22.0	8.3	–	–	–	–	–
084	LESS J033154.2–275109	03:31:54.22	–27:51:09.8	8.9	03:31:54.4937	–27:51:05.382	15.6 ± 1.8	5.7	0.039
					03:31:53.8248	–27:51:03.805	12.5 ± 1.6	8.0	(0.073)
085	LESS J033110.3–274503*	03:31:10.28	–27:45:03.1	7.7	–	–	–	–	–
086	LESS J033114.9–274844	03:31:14.90	–27:48:44.3	8.5	–	–	–	–	–
089	LESS J033248.4–280023	03:32:48.44	–28:00:23.8	9.1	–	–	–	–	–
090	LESS J033243.7–273554	03:32:43.65	–27:35:54.1	9.1	–	–	–	–	–
091	LESS J033135.2–274033	03:31:35.25	–27:40:33.7	9.1	–	–	–	–	–
092	LESS J033138.4–274336	03:31:38.36	–27:43:36.0	9.2	–	–	–	–	–
093	LESS J033110.8–275607*	03:31:10.84	–27:56:07.2	8.4	–	–	–	–	–
094	LESS J033307.3–275805	03:33:07.27	–27:58:05.0	9.1	03:33:07.5902	–27:58:05.840	7.9 ± 1.3	4.3	0.053
095	LESS J033241.7–275846	03:32:41.74	–27:58:46.1	9.2	03:32:41.2330	–27:58:41.239	16.0 ± 1.9	8.3	(0.062)
097	LESS J033313.7–273803	03:33:13.65	–27:38:03.4	9.2	–	–	–	–	–
099	LESS J033251.4–275536	03:32:51.45	–27:55:36.0	9.2	–	–	–	–	–
100	LESS J033111.3–280006*	03:31:11.32	–28:00:06.2	8.8	–	–	–	–	–

Table 3 – continued

ID	SMG name	Submm position		r_s (arcsec)	5.8- μ m position		5.8- μ m flux (μ Jy)	Offset (arcsec)	p
		(α_{J2000})	(δ_{J2000})		(α_{J2000})	(δ_{J2000})			
104	LESS J033258.5–273803	03:32:58.46	–27:38:03.0	9.4	03:32:58.2588	–27:38:11.522	8.9 ± 1.4	8.9	0.108
105	LESS J033115.8–275313	03:31:15.78	–27:53:13.1	9.0	03:32:57.8215	–27:37:59.117	7.6 ± 1.3	9.3	0.119
106	LESS J033140.1–275631	03:31:40.09	–27:56:31.4	9.4	03:31:40.1741	–27:56:22.412	39.3 ± 2.9	9.1	0.023
107	LESS J033130.8–275150	03:31:30.85	–27:51:50.9	9.4	03:31:30.5506	–27:51:58.716	10.8 ± 1.6	8.8	(0.095)
109	LESS J033328.1–274157	03:33:28.08	–27:41:57.0	9.5	03:33:28.0061	–27:42:02.408	11.5 ± 1.6	5.5	0.053
					03:33:28.5086	–27:41:50.420	7.7 ± 1.3	8.7	0.116
110	LESS J033122.6–275417	03:31:22.64	–27:54:17.2	9.4	03:31:22.6330	–27:54:17.014	6.8 ± 1.3	0.2	0.000
112	LESS J033249.3–273112	03:32:49.28	–27:31:12.3	9.0	03:32:48.8558	–27:31:12.868	24.5 ± 2.3	5.7	0.021
113	LESS J033236.4–275845	03:32:36.42	–27:58:45.9	9.5	–	–	–	–	–
115	LESS J033349.7–274239	03:33:49.71	–27:42:39.2	8.9	03:33:49.6663	–27:42:34.067	9.9 ± 1.6	5.2	0.053
116	LESS J033154.4–274525	03:31:54.42	–27:45:25.5	9.7	–	–	–	–	–
119	LESS J033256.5–280319	03:32:56.51	–28:03:19.1	9.7	–	–	–	–	–
121	LESS J033333.3–273449	03:33:33.32	–27:34:49.3	9.7	–	–	–	–	–
123	LESS J033330.9–275349	03:33:30.88	–27:53:49.3	9.8	–	–	–	–	–
124	LESS J033203.6–273605	03:32:03.59	–27:36:05.0	10.0	03:32:03.0814	–27:36:01.278	7.9 ± 1.3	7.7	0.109
					03:32:04.0070	–27:36:05.810	6.5 ± 1.2	5.6	(0.090)
125	LESS J033146.0–274621	03:31:46.02	–27:46:21.2	9.9	–	–	–	–	–
126	LESS J033209.8–274102	03:32:09.76	–27:41:02.0	9.9	03:32:09.6084	–27:41:06.983	12.0 ± 1.6	5.4	0.051

5.6 μ Jy). Below these S/N thresholds, the detections become less reliable (‘sources’ are increasingly likely to be noise spikes, residual side lobes, map artefacts, etc.) and automated source-finding algorithms such as SAD, used to form the catalogues, have greater difficulty in producing reliable fits to genuine sources, which are therefore rejected. A detailed examination of the radio and mid-IR sources shown in Fig. A1 can help to identify such cases, especially where there is coincident emission in both wavebands, and in Appendix A we give a brief description of any noteworthy SMGs. This includes likely blends of individual submm sources and possible counterparts that lie outside the search radius (along with their fluxes and positions).

Fainter SMGs should, broadly speaking, also be fainter in the radio and mid-IR (different spectral properties or their redshift dependency will of course weaken the correlation). Indeed, it is very apparent from Tables 1 and 2 that fewer SMGs have secure counterparts as you move to the bottom of the tables, i.e. towards decreasing S/N. This is illustrated in Fig. 6, where we plot the cumulative recovery fraction as a function of S/N (which, given the uniform noise in the LABOCA map, is strongly correlated with submm flux). At high S/N, there are few sources and the trend is very noisy, but as the S/N declines below 6 there is a clear trend towards a declining fraction of SMGs with secure counterparts, as expected.

Of the five SMGs with the highest S/N, only one has a radio source within the search radius. One of these, LESS004, can be seen in Fig. A1 to clearly be a blend of multiple sources. For the other sources, no such blend is obvious. Most striking is the brightest SMG in the LESS sample, LESS001, for which there is no radio emission at all and only extremely faint mid-IR emission within the search radius (although this is classed as the counterpart to the SMG). Blends do, of course, contribute doubly to this effect – their flux density is overestimated and the additional positional offsets render the identification of any counterpart more difficult. However, it is also possible that the reason for the lack of counterpart emission is due to the source lying at very high redshift (e.g. Ivison et al. 2002; Younger et al. 2007; Dannerbauer, Walter & Morrison 2008) or the dust in the galaxy being colder than average (Chapman et al. 2005).

6.3 Redshift distribution

Whilst the flux density of an SMG is essentially independent of redshift (up to $z \sim 8$), both the radio and IR emission will fade with increasing distance. The median spectroscopic redshift of radio-identified SMGs is 2.2 (Chapman et al. 2005), although the requirement that an accurate radio position be available (in order to place the slit accurately for the spectroscopic observations – see Ivison et al. 2005) may skew the redshift distribution towards a lower range. An increasing number of SMGs have been identified at $z > 4$ (Schinnerer et al. 2008; Daddi et al. 2009a,b; Knudsen et al. 2010), including one from this survey with a spectroscopically determined redshift of 4.76 (Coppin et al. 2009; Coppin et al. 2010): LESS073 (with $p = 0.003$ in Table 1).

We can investigate the redshift distribution of the radio-detected secure counterparts by utilizing the radio-to-submm spectral index relation (1.4:350 GHz, $\alpha_{1.4}^{350}$) of Carilli & Yun (2000, hereafter CY00) who characterize the variation of $\alpha_{1.4}^{350}$ with z using the average of 17 template spectral energy distributions (SEDs). The resulting redshifts are therefore averaged over various source properties including radio spectral index, α_{radio} , submm spectral index, α_{submm} , and dust temperature. In order to make our redshift estimates as reliable as possible, we have only included sources where the robust counterpart consists of only a single radio component. The resulting 55 redshifts are plotted in Fig. 7 and listed in Table 4; the 1σ errors include the uncertainties in the fluxes and the spread in the submm spectral index.

Our distribution is similar to those found by Chapman et al. (2005) and Wardlow et al. (2010) which are also plotted in Fig. 7. The median of our redshift distribution is $\bar{z} = 2.2_{-0.7}^{+0.8}$ (1σ errors), identical to both the spectroscopically derived median for the radio-identified SMGs of Chapman et al. (2005) and that measured by Wardlow et al. (2010) using 17-band optical to mid-IR photometry; Aretxaga et al. (2007) measure median redshifts of between 2.2 and 2.7 for the two SHADES fields. The Wardlow et al. (2010) study is particularly relevant as it uses the sample of robust counterparts identified in this work, although it is not confined to those with a radio detection. A comparison of the

Table 4. Summary of counterparts to SMGs. We show the deboosted submm, MIPS 24 μm and deboosted radio flux densities for each robust counterpart. Also included are the redshifts estimated from the submm/radio spectral index. LESS063 and 118 have not had redshifts calculated as the radio emission may be spurious. We have also not calculated the redshifts when there are multiple robust radio counterparts.

SMG	870 μm (mJy)	24 μm (μJy)	21 cm (μJy)	z	SMG	870 μm (mJy)	24 μm (μJy)	21 cm (μJy)	z
001	13.8 ± 1.1	38.0 ± 7.9	–	–	056	4.5 ± 1.4	270.3 ± 11.4	31.8 ± 6.5	$2.82^{+1.69}_{-0.92}$
002	11.5 ± 1.2	61.7 ± 18.3	234.6 ± 7.8	$1.62^{+0.68}_{-0.39}$	057	4.6 ± 1.5	297.2 ± 8.4	49.4 ± 6.7	$2.21^{+1.20}_{-0.64}$
	–	186.5 ± 22.6	–	–	059	4.4 ± 1.5	172.1 ± 10.6	–	–
003	11.3 ± 1.2	33.6 ± 7.4	–	–	060	4.3 ± 1.4	292.8 ± 9.8	64.7 ± 6.9	$1.86^{+0.89}_{-0.48}$
006	9.1 ± 1.2	35.7 ± 9.6	42.7 ± 7.4	$3.67^{+2.33}_{-1.32}$	062	4.4 ± 1.5	243.5 ± 35.6	151.2 ± 7.3	$1.32^{+0.45}_{-0.31}$
007	8.6 ± 1.2	368.3 ± 8.1	75.8 ± 6.9	$2.47^{+1.41}_{-0.76}$	063	4.3 ± 1.5	–	31.8 ± 7.2	–
009	8.6 ± 1.3	110.6 ± 10.6	31.0 ± 6.3	$4.38^{+2.84}_{-1.63}$	064	4.2 ± 1.4	338.4 ± 17.2	23.6 ± 6.2	$3.26^{+2.03}_{-1.13}$
010	8.5 ± 1.3	119.8 ± 18.0	54.9 ± 6.0	–	066	4.4 ± 1.6	543.7 ± 12.3	67.0 ± 7.8	$1.85^{+0.88}_{-0.48}$
		–	51.1 ± 6.1	–	067	4.2 ± 1.5	516.4 ± 8.0	90.1 ± 14.8	$1.59^{+0.65}_{-0.38}$
		–	50.1 ± 6.2	–	070	4.1 ± 1.4	365.2 ± 17.4	322.3 ± 14.6	$0.96^{+0.31}_{-0.31}$
011	8.4 ± 1.3	103.1 ± 8.4	55.1 ± 6.6	$2.95^{+1.80}_{-0.98}$	072	4.1 ± 1.4	471.4 ± 22.9	34.3 ± 7.1	$2.55^{+1.47}_{-0.80}$
012	8.1 ± 1.3	43.2 ± 8.8	39.9 ± 6.5	$3.55^{+2.25}_{-1.26}$	073	4.1 ± 1.4	15.2 ± 6.9	18.9 ± 5.1	$3.71^{+2.37}_{-1.33}$
014	8.6 ± 1.4	95.5 ± 9.5	89.4 ± 8.0	$2.25^{+1.23}_{-0.65}$	074	4.2 ± 1.5	202.0 ± 23.4	43.8 ± 7.5	–
015	8.1 ± 1.4	108.6 ± 10.1	–	–			–	34.8 ± 7.0	–
016	7.4 ± 1.3	457.3 ± 15.9	49.0 ± 8.5	$2.94^{+1.78}_{-0.98}$	075	4.2 ± 1.5	1018.1 ± 38.3	72.3 ± 8.2	$1.75^{+0.79}_{-0.44}$
017	6.9 ± 1.3	219.3 ± 7.7	120.3 ± 14.5	$1.74^{+0.78}_{-0.43}$	076	4.2 ± 1.5	–	41.6 ± 8.4	$2.31^{+1.28}_{-0.68}$
018	6.7 ± 1.3	560.5 ± 8.2	130.1 ± 17.3	$1.66^{+0.71}_{-0.40}$	078	4.2 ± 1.7	369.3 ± 43.0	75.2 ± 9.8	$1.72^{+0.76}_{-0.43}$
019	6.5 ± 1.3	79.8 ± 7.5	30.8 ± 6.0	$3.64^{+2.32}_{-1.30}$	079	3.8 ± 1.4	520.7 ± 9.2	34.8 ± 6.3	$2.42^{+1.36}_{-0.73}$
		40.0 ± 8.6	–	–	081	3.8 ± 1.5	523.6 ± 11.0	217.9 ± 15.3	$1.10^{+0.33}_{-0.31}$
020	6.4 ± 1.3	176.6 ± 7.6	4251.9 ± 16.0	$0.09^{+0.24}_{-0.09}$	084	3.7 ± 1.4	133.5 ± 7.3	33.5 ± 6.1	$2.43^{+1.38}_{-0.74}$
022	7.2 ± 1.6	409.8 ± 12.7	111.3 ± 25.3	$1.84^{+0.87}_{-0.47}$	087	4.2 ± 1.9	419.4 ± 13.2	128.3 ± 25.8	–
024	6.6 ± 1.5	130.2 ± 9.3	60.0 ± 8.1	$2.43^{+1.37}_{-0.74}$				56.9 ± 8.7	–
025	5.9 ± 1.3	233.2 ± 8.0	61.3 ± 7.3	$2.25^{+1.23}_{-0.65}$	088	3.6 ± 1.4	269.5 ± 19.4	78.0 ± 6.6	$1.58^{+0.65}_{-0.37}$
027	6.3 ± 1.5	171.9 ± 16.4	–	–	094	3.5 ± 1.4	106.2 ± 7.3	–	–
		277.3 ± 18.8	–	–	096	3.4 ± 1.4	961.6 ± 9.0	80.6 ± 17.4	$1.53^{+0.59}_{-0.36}$
029	6.2 ± 1.6	136.0 ± 9.2	44.7 ± 8.6	$2.79^{+1.66}_{-0.91}$			33.1 ± 7.6	–	–
031	5.5 ± 1.4	66.2 ± 9.0	25.9 ± 5.8	$3.66^{+2.33}_{-1.31}$	098	3.3 ± 1.4	268.8 ± 15.7	141.8 ± 8.1	$1.22^{+0.38}_{-0.30}$
034	5.5 ± 1.4	223.3 ± 9.4	–	–	101	3.3 ± 1.4	43.9 ± 6.6	25.3 ± 6.1	$2.68^{+1.59}_{-0.85}$
035	7.2 ± 2.0	73.3 ± 9.6	–	–	102	3.4 ± 1.5	318.4 ± 16.5	–	–
036	5.5 ± 1.5	274.5 ± 9.6	47.5 ± 7.5	$2.50^{+1.44}_{-0.77}$	103	3.4 ± 1.5	113.3 ± 13.5	–	–
037	5.8 ± 1.6	201.8 ± 19.7	–	–	105	3.6 ± 1.7	–	–	–
039	5.3 ± 1.5	131.0 ± 7.5	45.9 ± 7.5	$2.50^{+1.43}_{-0.77}$	106	3.2 ± 1.3	363.6 ± 10.2	66.8 ± 7.1	$1.61^{+0.67}_{-0.39}$
040	5.0 ± 1.4	119.8 ± 7.2	119.1 ± 13.7	$1.52^{+0.60}_{-0.35}$	108	3.1 ± 1.3	3722.6 ± 73.7	379.7 ± 36.4	$0.78^{+0.30}_{-0.33}$
041	6.7 ± 2.0	241.8 ± 20.8	–	–	109	3.1 ± 1.4	169.0 ± 15.5	24.6 ± 6.6	$2.63^{+1.54}_{-0.83}$
043	5.0 ± 1.5	229.6 ± 7.2	–	–	110	3.2 ± 1.5	–	–	–
044	5.8 ± 1.8	400.9 ± 13.0	90.3 ± 9.6	$1.83^{+0.87}_{-0.47}$	111	3.2 ± 1.4	353.7 ± 53.3	54.0 ± 9.4	$1.77^{+0.80}_{-0.45}$
045	4.9 ± 1.4	116.1 ± 8.1	31.1 ± 5.9	$3.01^{+1.85}_{-1.01}$	112	3.6 ± 1.9	190.8 ± 13.2	29.6 ± 8.0	$2.57^{+1.50}_{-0.80}$
046	6.3 ± 1.9	–	73.2 ± 10.7	$2.12^{+1.12}_{-0.59}$	114	3.0 ± 1.3	515.0 ± 7.8	95.4 ± 6.7	$1.36^{+0.47}_{-0.32}$
047	5.4 ± 1.6	–	–	–	115	3.7 ± 2.2	–	–	–
048	5.9 ± 1.8	406.8 ± 11.9	84.5 ± 8.3	$1.91^{+0.93}_{-0.50}$	117	3.0 ± 1.4	203.1 ± 13.1	81.0 ± 8.4	$1.45^{+0.54}_{-0.34}$
049	5.0 ± 1.5	122.9 ± 11.6	36.0 ± 7.2	–	118	3.0 ± 1.4	–	23.5 ± 6.3	–
		113.5 ± 14.6	115.9 ± 19.1	–	120	2.9 ± 1.4	345.6 ± 9.5	45.5 ± 8.4	$1.83^{+0.85}_{-0.47}$
050	4.7 ± 1.4	306.6 ± 24.1	77.3 ± 7.2	$1.79^{+0.82}_{-0.46}$	122	2.8 ± 1.3	1392.5 ± 15.8	207.3 ± 14.5	$0.99^{+0.31}_{-0.31}$
		64.4 ± 12.3	–	–	126	2.8 ± 1.3	263.4 ± 8.7	23.3 ± 5.5	$2.56^{+1.48}_{-0.80}$
054	5.0 ± 1.6	222.1 ± 8.8	–	–					

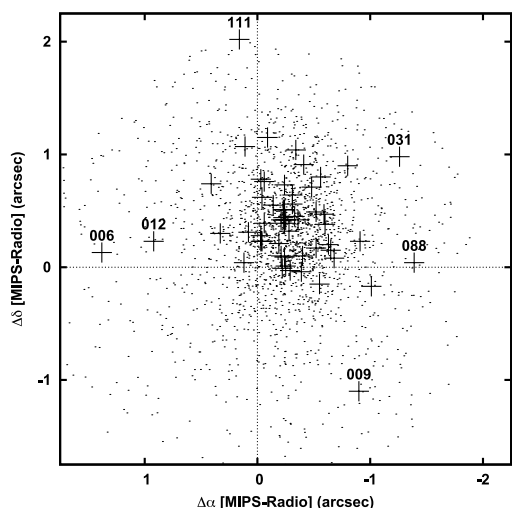


Figure 4. Offsets (arcsec) in right ascension and declination between the MIPS and radio counterpart positions (large crosses) with the largest offsets marked with the relevant SMG. Also plotted are the offsets for 2019 matches between the radio and MIPS catalogues – the median offset is equal to -0.25 arcsec in right ascension and $+0.29$ arcsec in declination (MIPS – radio) and the plot is centred on these coordinates.

redshifts measured here and by Wardlow et al. (2010) is shown in Fig. 8.

There are a number of significant outliers, perhaps the most obvious of which is LESS020, for which the CY00 technique gives a much lower value of $z = 0.09$ compared to 2.8 from the full photometric analysis. This is by far the brightest of the radio counterparts ($S_{1.4} > 4$ mJy) and its radio flux is most likely boosted by a radio-loud active galactic nucleus (AGN) for which the SED templates of CY00 do not apply. The other most prominent outlier is LESS006, for which there is a large offset between the $24\ \mu\text{m}$ and radio positions and where the radio emission lies predominantly between two peaks in the $3.6\text{-}\mu\text{m}$ image (Fig. A1). Based on the large (> 1 arcsec) positional offsets, Wardlow et al. (2010) suggest

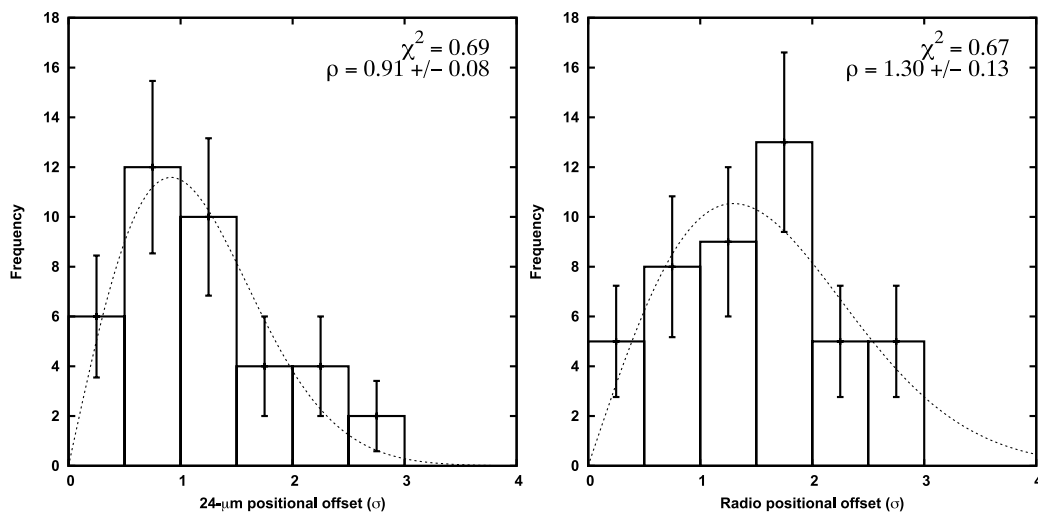


Figure 5. Distribution of positional offsets (in units of σ) from the submm position for the radio (right) and $24\text{-}\mu\text{m}$ (left) sources with $p \leq 0.05$; error bars are Poissonian. The dashed line shows a fitted Rayleigh distribution [$R(r) \propto r e^{-r^2/2\rho^2}$], where r is the radial offset and ρ the standard deviation of the positional errors in either right ascension (or declination, the two being equal). The reduced chi-squared of the fit (χ^2) and the value of ρ are given in the top-right-hand corner. For the MIPS counterparts, the offsets conform closely to the expected distribution and ρ is close to the expected value. For the radio, despite removing the astrometric offset seen in Fig. 4, it is possible that there are more radio counterparts at larger radii than expected.

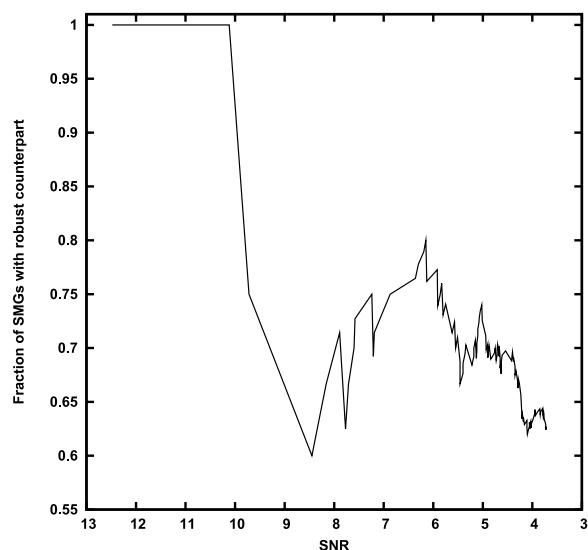


Figure 6. Cumulative recovery fraction of secure radio and MIPS counterparts per SMG as a function of S/N. Below an S/N of about 6, there is a steady decline in the fraction of SMGs with robust counterparts, as expected. At higher S/N, the trend is noisier and two of the five brightest SMGs do not have identifications.

that this SMG is being gravitationally lensed by the low-redshift ($z = 0.4$) optical/mid-IR galaxy and the much larger redshift ($z = 3.7$) measured based on the radio/submm flux would support this conclusion. Excluding these two outliers results in a Spearman rank correlation coefficient of 0.43 which, for 48 common redshifts, easily exceeds the critical value (0.24) for 95 per cent significance and allows us to reject the hypothesis that there is no correlation.

The excellent agreement in the measurement of the median redshift of the SMG population, using three different techniques, is very encouraging and strongly argues that the peak in SMG activity was at or close to $z = 2.2$. However, in all three cases, the majority of the redshifts were made possible due to the presence of radio emission, in the Chapman et al. (2005) case as an indicator of

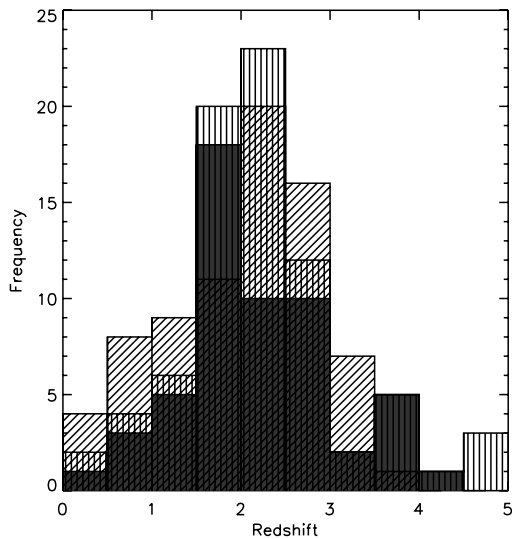


Figure 7. Left: the solid filled histogram shows the redshift distribution calculated using the radio/submm spectral index relation of Carilli & Yun (2000); this includes all 55 robust counterparts from Tables 1, 2 and 3 that have a single, robust radio detection. The median of the distribution is 2.2 with an interquartile range of 1.6–2.6. Also shown are the redshift distributions of (diagonal hatch) Chapman et al. (2005) and (vertical hatch) Wardlow et al. (2010). None of the distributions has been scaled – the y-axis shows the actual number of redshifts in each case.

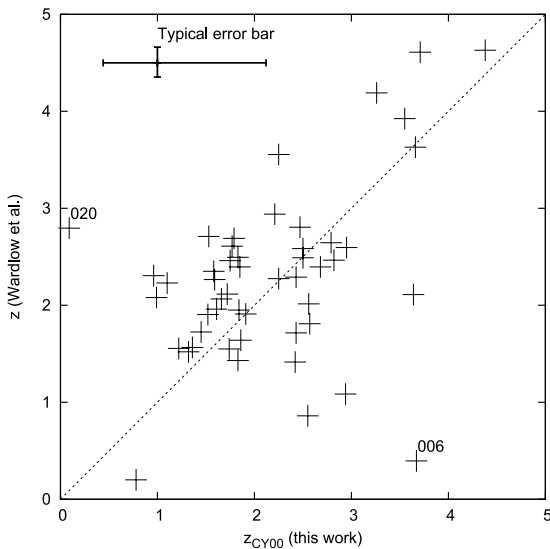


Figure 8. A comparison between the redshifts measured for sources common to Wardlow et al. (2010) and this work. Error bars have been omitted for clarity, but a typical error bar is shown in the top-left corner. The Spearman rank correlation coefficient is equal to 0.43 (significant at >95 per cent confidence), which confirms that there is a positive correlation between the two redshift measures.

where to place the spectroscopic slit. Because of the fading of radio emission with increased distance (positive k -correction) this means that many of the SMGs in these samples which are not detected in the radio, the majority of which remain unidentified, are likely to be biased towards higher redshifts. Indeed, the majority of the LESS sample are undetected in the radio and although some of these will be undetected because they are unusually cold, overall we expect this radio-faint subsample to have a redshift distribution skewed to larger values than the radio-detected SMGs. It is thus possible

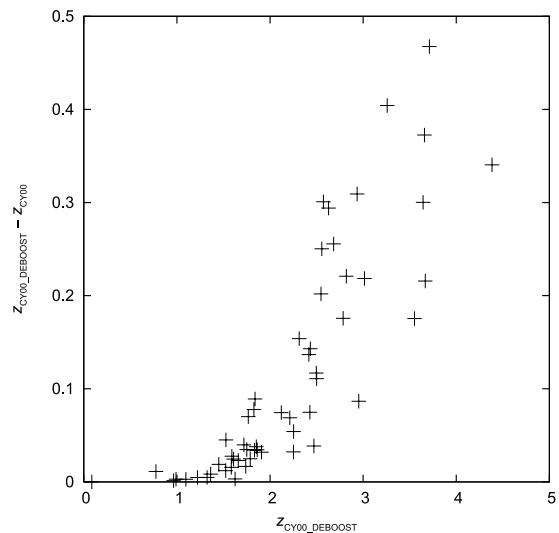


Figure 9. Increase in the measured CY00 redshift caused by using deboosted flux densities. The increase can be significant (≤ 0.5) and is most pronounced at high redshifts (high redshifts are biased towards weaker radio flux densities which are in turn most affected by flux boosting).

that the overall median redshift of our SMG sample is higher than 2.2 although we note that there is an additional bias in the other direction – the IRAC counterparts are preferentially located at high redshift as they have weak radio emission and lie in the high-redshift quadrant of the Pope et al. (2006) diagram (Fig. 3).

The use of deboosted radio flux densities also has the effect of increasing the redshifts measured using the CY00 technique. This is demonstrated in Fig. 9 where we plot the CY00 redshifts measured using both deboosted and undeboosted radio flux densities. The increase due to the deboosting is most pronounced at the highest redshifts which, for a given submm flux density, correspond to the weaker radio sources that are most affected by flux boosting. Whilst the majority of the SMGs have $\Delta z < 0.1$, the maximum increase is $\lesssim 0.5$, this is corresponding to the only source for which we have a spectroscopic redshift (LESS073 at $z = 4.76$). The CY00 redshift is 3.7, a considerable improvement on the value of 3.2 that would otherwise have been measured without the use of deboosted radio fluxes. Overall, the combined effect is to increase the median redshift of the SMGs by 0.2 i.e. from 2.0 to 2.2.

In Fig. 10 we have plotted deboosted submm flux density as a function of Carilli–Yun redshift. Also shown are the median redshifts of the data in four separate flux-density bins. This reveals an increase in the average flux density with redshift, an effect previously noted by Ivison et al. (2002), Pope et al. (2005) and Younger et al. (2008). The 870- μm flux density of Arp 220 is also plotted in Fig. 10, as a function of redshift, to illustrate that the apparent evolution of SMG luminosity with redshift (note that Wardlow et al. 2010 do not find evidence for such an effect) is unlikely to be caused by their SEDs, or by cosmology. The Spearman rank correlation coefficient, with LESS020 and LESS006 again excluded, is equal to 0.39 which allows us to reject the null hypothesis with >95 per cent confidence (the critical value for 53 pairs is equal to 0.23).

The exact form of the evolution of SMGs with redshift remains unclear (e.g. Chapin, Hughes & Aretxaga 2009b), particularly whether it is predominantly in luminosity, density or both, but there are signs that luminosity evolution plays a role. Wall, Pope & Scott (2008) have even suggested that there are in fact two populations of SMGs, separated by luminosity, and that these evolve

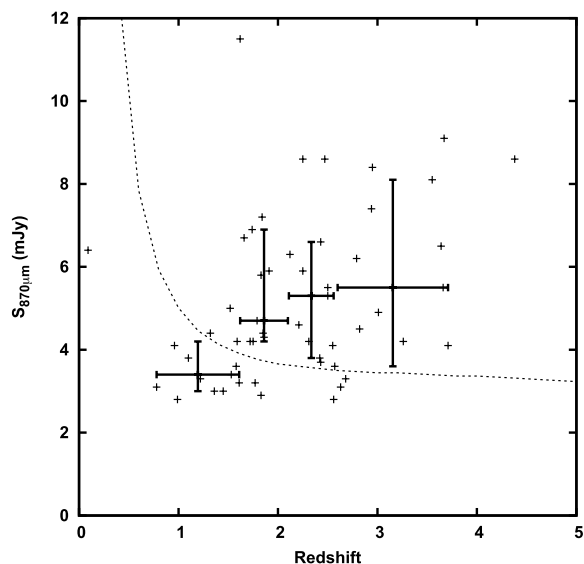


Figure 10. Deboosted submm flux density versus redshifts calculated using the Carilli–Yun radio/submm spectral index relation. Superimposed are the median flux densities in four redshift bins; each bin contains 13 or 14 sources. Error bars are 1σ . Also shown is the 870- μm flux density of Arp 220 as a function of redshift (dashed line) normalized to the lowest redshift bin’s average. As can be seen, there is a weak trend of increasing flux at higher redshifts – the Spearman rank correlation coefficient for the unbinned data is 0.39 which is significant at >95 per cent confidence.

differently. It is therefore tempting to ascribe the lack of detections of the brightest SMGs as being due to their high redshifts. However, it is equally possible that the brightest galaxies arise due to confusion from clustering in the brightest sources, or from temperature and luminosity evolution which results in them being high-luminosity, low-temperature galaxies at low redshift.

7 CONCLUSIONS

Using a probabilistic approach, we have attempted to identify reliable counterparts to the 126 SMGs recently discovered at a wavelength of 870 μm in the LESS survey of the ECDF-S using the LABOCA camera on the APEX telescope (Weiß et al. 2009). Taking values of the corrected Poissonian probability (the so-called p -statistic, p) that are less than or equal to 0.05 to indicate a secure identification, i.e. a highly unlikely chance coincidence, we have found reliable radio and/or 24- μm counterparts to 62 SMGs. A further 17 SMGs were identified using IRAC sources that fell within a colour-flux cut that was constructed from the results of the radio and MIPS analysis. In contrast to most previous work of a similar nature, we have based our identifications on rigorously constructed catalogues of 1.4-GHz and MIPS/IRAC sources.

In total, we find that 79 out of the 126 SMGs have secure counterparts, an identification fraction of 63 per cent. This is not as high as some other studies, partly due to the relatively shallow radio map and somewhat larger submm beam. In several cases, it is obvious that multiple submm emitters are blended and consequently difficult to identify.

Finally, in creating our radio catalogue, we have performed simulations in order to correct the flux densities for ‘flux boosting’. This has particular relevance to the calculation of source redshifts based on the radio-submm spectral index, a technique which often uses deboosted submm fluxes, but ignores the corresponding effect in the radio. With the systematic shift towards lower redshifts removed,

the median redshift of the radio-detected SMGs in our sample is $\bar{z} = 2.2^{+0.8}_{-0.7}$ (1σ errors). This is identical to that found by both Chapman et al. (2005) and Wardlow et al. (2010), the latter using the sample of SMGs identified in this paper, but using a different technique (optical to mid-IR multiband photometry) for measuring the source redshifts. The median redshift of the full sample is likely to be rather higher as the unidentified SMGs by definition have weak radio emission.

The current generation of submm cameras produce maps with such poor resolution that a probabilistic approach to identifying SMGs is inevitable. Ideally, identification work such as that presented in this paper would be done with telescopes offering subarc-second resolution, such as the IRAM Plateau de Bure Interferometer and the SMA. However, due to their limited sensitivity (small numbers of antennas and relatively poor atmospheric transmission), many hours are required for a reliable detection of a typical SMG. In the future, ALMA will revolutionize the study of high-redshift star formation with its order of magnitude increase in sensitivity and imaging fidelity which will make pinpointing the origin of the submm emission in surveys such as LESS a relatively trivial exercise, requiring only minutes per source to achieve a high dynamic range image.

ACKNOWLEDGMENTS

The authors would like to acknowledge the comments provided by the anonymous referee that significantly improved the manuscript. The National Radio Astronomy Observatory is a facility of the National Science Foundation operated under cooperative agreement by Associated Universities, Inc. This work is based in part on observations made with the *Spitzer Space Telescope*, which is operated by the Jet Propulsion Laboratory, California Institute of Technology under a contract with NASA. We thank Jacqueline Monkiewicz and the FIDEL team for the *Spitzer* 24- μm data reductions. JLW acknowledges the receipt of an STFC studentship. IS acknowledges support from the STFC. This research has made use of the NASA/IPAC Extragalactic Data base (NED) which is operated by the Jet Propulsion Laboratory, California Institute of Technology, under contract with the National Aeronautics and Space Administration. ADB would like to thank Phillip Helbig for the use of his cosmology code.

REFERENCES

- Aretxaga I. et al., 2007, MNRAS, 379, 1571
- Austermann J. E. et al., 2009, MNRAS, 393, 1573
- Barger A. J., Cowie L. L., Sanders D. B., Fulton E., Taniguchi Y., Sato Y., Kawara K., Okuda H., 1998, Nat, 394, 248
- Beckwith S. V. W. et al., 2006, AJ, 132, 1729
- Bertin E., Arnouts S., 1996, A&AS, 117, 393
- Bertoldi F. et al., 2007, ApJS, 172, 132
- Biggs A. D., Ivison R. J., 2006, MNRAS, 371, 963
- Bondi M. et al., 2003, A&A, 403, 857
- Browne I. W. A., Cohen A. M., 1978, MNRAS, 182, 181
- Carilli C. L., Yun M. S., 1999, ApJ, 513, L13
- Carilli C. L., Yun M. S., 2000, ApJ, 530, 618
- Chapin E. L. et al., 2009a, MNRAS, 398, 1793
- Chapin E. L., Hughes D. H., Aretxaga I., 2009b, MNRAS, 393, 653
- Chapman S. C., Blain A. W., Smail I., Ivison R. J., 2005, ApJ, 622, 772
- Chary R. et al., 2004, ApJS, 154, 80
- Condon J. J., 1992, ARA&A, 30, 575
- Coppin K. et al., 2006, MNRAS, 372, 1621
- Coppin K. E. K. et al., 2009, MNRAS, 395, 1905
- Coppin K. E. K. et al., 2010, MNRAS, 407, 103

- Cowie L. L., Barger A. J., Wang W., Williams J. P., 2009, *ApJ*, 697, L122
- Daddi E., Dannerbauer H., Krips M., Walter F., Dickinson M., Elbaz D., Morrison G. E., 2009a, *ApJ*, 695, L176
- Daddi E. et al., 2009b, *ApJ*, 694, 1517
- Damen M. et al., 2011, *ApJ*, 727, 1
- Dannerbauer H., Lehnert M. D., Lutz D., Tacconi L., Bertoldi F., Carilli C., Genzel R., Menten K. M., 2004, *ApJ*, 606, 664
- Dannerbauer H., Walter F., Morrison G., 2008, *ApJ*, 673, L127
- Downes A. J. B., Peacock J. A., Savage A., Carrie D. R., 1986, *MNRAS*, 218, 31
- Downes D. et al., 1999, *A&A*, 347, 809
- Eales S., Lilly S., Gear W., Dunne L., Bond J. R., Hammer F., Le Fèvre O., Crampton D., 1999, *ApJ*, 515, 518
- Elbaz D., Cesarsky C. J., Chantal P., Aussel H., Franceschini A., Fadda D., Chary R. R., 2002, *A&A*, 384, 848
- Fazio G. G. et al., 2004, *ApJS*, 154, 10
- Fixsen D. J., Dwek E., Mather J. C., Bennett C. L., Shafer R. A., 1998, *ApJ*, 508, 123
- Frayer D. T. et al., 2006, *ApJ*, 647, L9
- Frayer D. T. et al., 2009, *AJ*, 138, 1261
- Gear W. K., Lilly S. J., Stevens J. A., Clements D. L., Webb T. M., Eales S. A., Dunne L., 2000, *MNRAS*, 316, L51
- Giacconi R. et al., 2001, *ApJ*, 551, 624
- Giavalisco M. et al., 2004, *ApJ*, 600, L93
- Greve T. R., Pope A., Scott D., Ivison R. J., Borys C., Conselice C. J., Bertoldi F., 2008, *MNRAS*, 389, 1489
- Greve T. R. et al., 2010, *ApJ*, 719, 483
- Güsten R., Nyman L. Å., Schilke P., Menten K., Cesarsky C., Booth R., 2006, *A&A*, 454, L13
- Hatsukade B. et al., 2010, *ApJ*, 711, 974
- Hinshaw G. et al., 2009, *ApJS*, 180, 225
- Holland W. S. et al., 1999, *MNRAS*, 303, 659
- Hughes D. H. et al., 1998, *Nat*, 394, 241
- Ibar E., Ivison R. J., Biggs A. D., Lal D. V., Best P. N., Green D. A., 2009, *MNRAS*, 397, 281
- Iono D. et al., 2006, *ApJ*, 640, L1
- Ivison R. J., Smail I., Le Borgne J.-F., Blain A. W., Kneib J.-P., Bezecourt J., Kerr T. H., Davies J. K., 1998, *MNRAS*, 298, 583
- Ivison R. J., Smail I., Barger A. J., Kneib J.-P., Blain A. W., Owen F. N., Kerr T. H., Cowie L. L., 2000, *MNRAS*, 315, 209
- Ivison R. J. et al., 2002, *MNRAS*, 337, 1
- Ivison R. J. et al., 2005, *MNRAS*, 364, 1025
- Ivison R. J. et al., 2007, *MNRAS*, 380, 199
- Ivison R. J. et al., 2008, *MNRAS*, 390, 1117
- Ivison R. J. et al., 2010, *MNRAS*, 402, 245
- Knudsen K. K., Kneib J., Richard J., Petitpas G., Egami E., 2010, *ApJ*, 709, 210
- Lehmer B. D. et al., 2005, *ApJS*, 161, 21
- Lonsdale C. J. et al., 2003, *PASP*, 115, 897
- Luo B. et al., 2008, *ApJS*, 179, 19
- Makovoz D., Moshir M., Laher R., Marsh K., 2002, in Bohlender D. A., Durand D., Handley T. H., eds, *ASP Conf. Ser. Vol. 281, Astronomical Data Analysis Software and Systems XI*. Astron. Soc. Pac., San Francisco, p. 417
- Miller N. A., Fomalont E. B., Kellermann K. I., Mainieri V., Norman C., Padovani P., Rosati P., Tozzi P., 2008, *ApJS*, 179, 114
- Owen F. N., Morrison G. E., 2008, *AJ*, 136, 1889
- Pope A., Borys C., Scott D., Conselice C., Dickinson M., Mobasher B., 2005, *MNRAS*, 358, 149
- Pope A. et al., 2006, *MNRAS*, 370, 1185
- Rieke G. H. et al., 2004, *ApJS*, 154, 25
- Schinnerer E. et al., 2008, *ApJ*, 689, L5
- Scott K. S. et al., 2008, *MNRAS*, 385, 2225
- Scott K. S. et al., 2010, *MNRAS*, 405, 2260
- Seymour N., McHardy I. M., Gunn K. F., 2004, *MNRAS*, 352, 131
- Siringo G. et al., 2009, *A&A*, 497, 945
- Smail I., Ivison R. J., Blain A. W., 1997, *ApJ*, 490, L5
- Smail I., Ivison R. J., Owen F. N., Blain A. W., Kneib J., 2000, *ApJ*, 528, 612
- Surace J. A. et al., 2005, *The SWIRE Data Release 2: Image Atlases and Source Catalogs for ELAIS-N1, ELAIS-N2, XMM-LSS, and the Lockman Hole*, Technical report. Spitzer Science Centre, Pasadena
- Taylor M. B., 2005, in Shopbell P., Britton M., Ebert R., eds, *ASP Conf. Ser. Vol. 347, Astronomical Data Analysis Software and Systems XIV*. Astron. Soc. Pac., San Francisco, p. 29
- Wall J. V., Pope A., Scott D., 2008, *MNRAS*, 383, 435
- Wang W., Cowie L. L., van Sadlers J., Barger A. J., Williams J. P., 2007, *ApJ*, 670, L89
- Wardlow J. L. et al., 2010, *MNRAS*, submitted
- Weiß A. et al., 2009, *ApJ*, 707, 1201
- Werner M. W. et al., 2004, *ApJS*, 154, 1
- Wilson G. W. et al., 2008, *MNRAS*, 386, 807
- Younger J. D. et al., 2007, *ApJ*, 671, 1531
- Younger J. D. et al., 2008, *MNRAS*, 387, 707

APPENDIX A: DETAILED DESCRIPTION OF SMGS

Here we give short descriptions of those SMGs that merit further discussion; postage stamp maps of each SMG are shown in Fig. A1.

(LESS001) *LESS J033314.3–275611*: the brightest of the SMGs has no nearby radio emission, but an extremely faint MIPS component (with associated IRAC emission) is classed as a robust counterpart.

(LESS002) *LESS J033302.5–275643*: high significance radio and 24- μm counterparts, but their positions are not coincident. An extension of the 24- μm emission passes under the radio source and the DAOPHOT catalogue has detected this as a weak source ($S/N < 3.5$); the redshift has been calculated assuming the weaker, but coincident, MIPS source is the correct counterpart to the radio. There is also an IRAC source at this position.

(LESS004) *LESS J033136.0–275439*: the p -statistic finds nothing, but this is likely due to the catalogued SMG being a blend of up to four sources, three of which have similar brightnesses. The northernmost of these three is coincident with a 76- μJy radio source. To the south, this chain of galaxies continues into LESS026.

(LESS006) *LESS J033257.1–280102*: both the radio and MIPS robust counterparts are weak, but separated by ~ 1 arcsec. The radio source appears to be extended, the eastern end of which lies closer to the MIPS position.

(LESS008) *LESS J033205.1–273108*: the nearest radio source beyond the search radius has a position of 03:32:04.8146, –27:31:14.143, a flux of 69 μJy and is offset by 6.3 arcsec from the nominal submm position.

(LESS010) *LESS J033219.0–275219*: the radio source gives the impression of having a bright core and a three-component jet. However, the end of the ‘jet’ corresponds to a 24- μm source and another of the ‘jet’ components is coincident with an IRAC source; the ‘core’ also has 24- μm emission. The SMG emission continues to the south-west where it merges into LESS034. This rather confusing source has not had a redshift calculated.

(LESS012) *LESS J033248.1–275414*: the bright MIPS source has a weak extension that DAOPHOT resolves into separate components; one of these lies less than 1 arcsec from the secure radio counterpart.

(LESS015) *LESS J033333.4–275930*: this SMG is a close neighbour of LESS076. The robust counterpart at 24 μm has associated weak radio emission.

(LESS019) *LESS J033208.1–275818*: both IRAC identifications have faint emission at 24 μm .

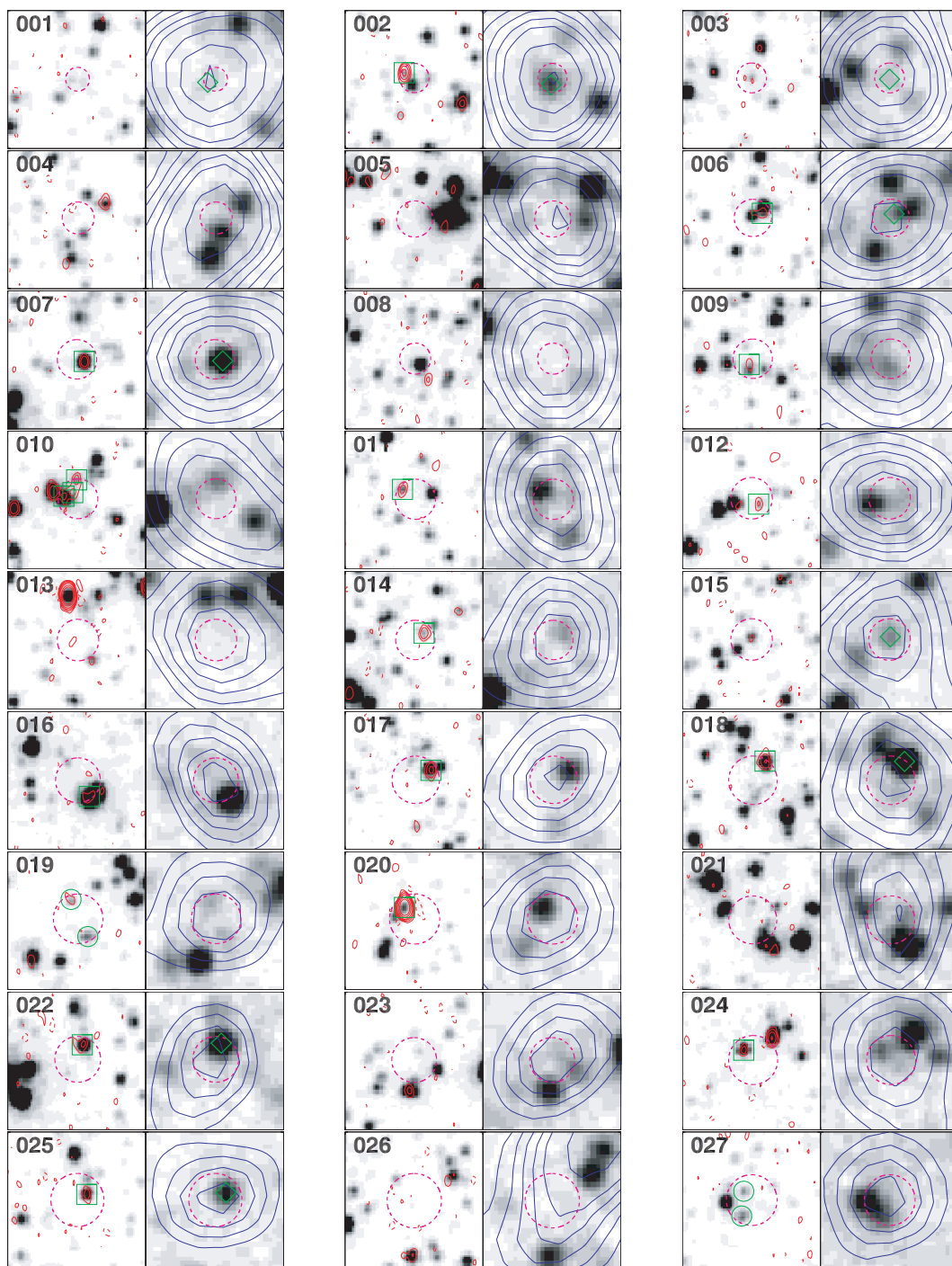
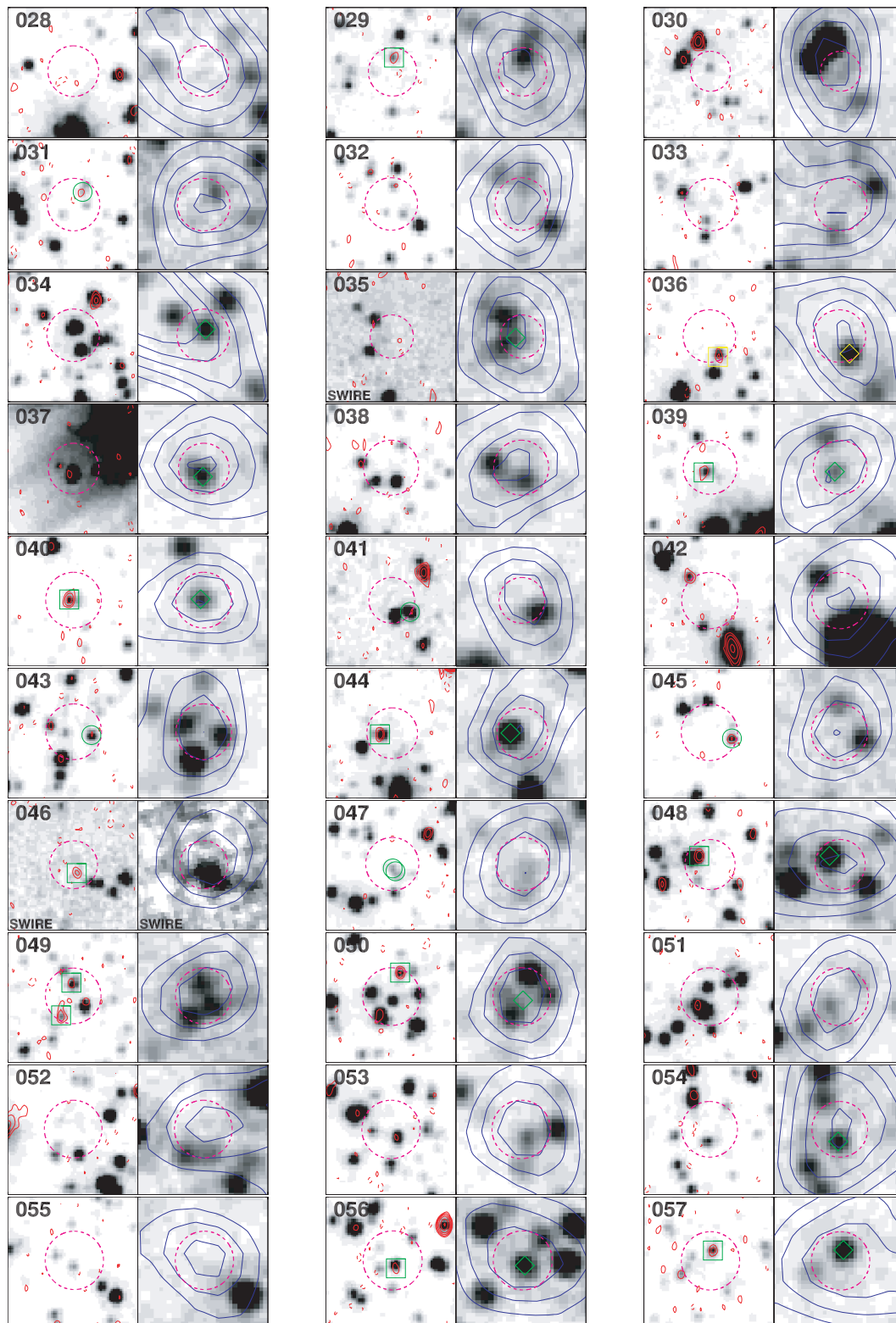


Figure A1. Plots centred on the location of each LABOCA-detected source in the ECDF-S; each is $36 \times 36 \text{ arcsec}^2$. Left-hand panel: 3.6- μm IRAC grey-scale image with radio 21-cm contours overlaid. Right-hand panel: 24- μm MIPS grey-scale with submm contours (S/N) overlaid. The radio images have all been shifted by 0.25 arcsec to the east and by 0.29 arcsec to the north (Section 6.1). The circle shows the search radius used to search for counterparts. Secure identifications ($p \leq 0.05$) are indicated by green squares (radio), diamonds (24 μm) and circles (5.8 μm). Paired yellow symbols represent those counterparts that are considered robust based on coincident emission having $0.05 < p \leq 0.1$ in two separate wavebands. Radio contours are plotted at $-3, 3, 5, 10, 20, 50$ and 100 times the 1σ rms noise. 870- μm contours are plotted at $2, 3, 4, 5, 6, 8, 10, 12, 14$ times the 1σ rms noise. Please note that the submm contours correspond to the beam-smoothed map that was used to identify the SMGs: see Weiß et al. (2009) for details. LESS046 is not located on the FIDEL 24- μm or the SIMPLE 3.6- μm images and so we have instead plotted the shallower SWIRE (Lonsdale et al. 2003) data for both. The SWIRE data have also been substituted for LESS035, 085, 093 and 100 at 3.6 μm .

Figure A1 – *continued*

(LESS020) *LESS J033316.6–280018*: this has by far the brightest of the robust radio counterparts, >4 mJy, and therefore probably contains a radio-loud AGN component. For this reason, the CY00 redshift is greatly in error.

(LESS023) *LESS J033212.1–280508*: the nearest radio source beyond the search radius has a flux of $65 \mu\text{Jy}$ at position $03:32:12.2230, -28:05:16.752$ and is associated with an obvious $24\text{-}\mu\text{m}$ source ($245 \mu\text{Jy}$).

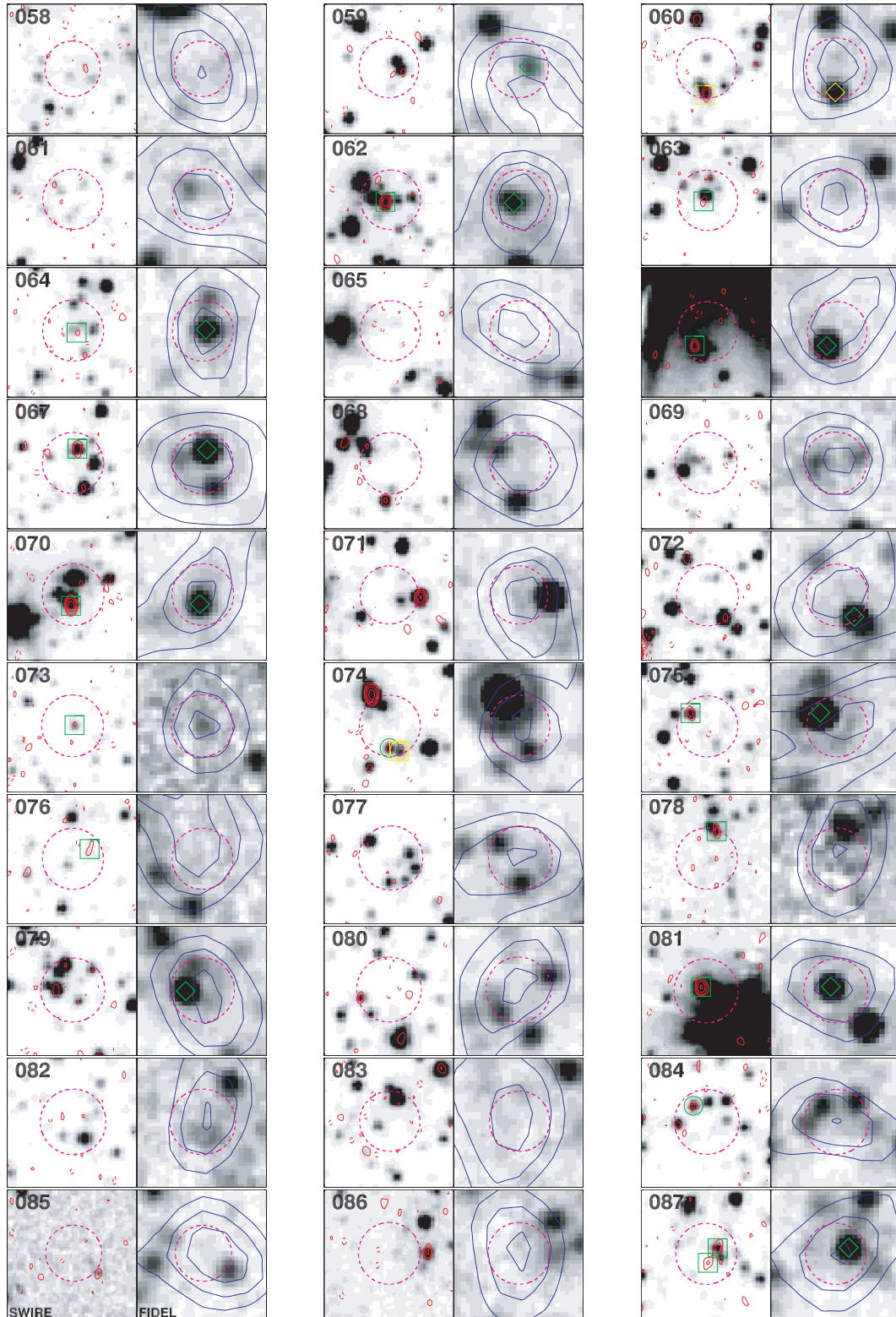
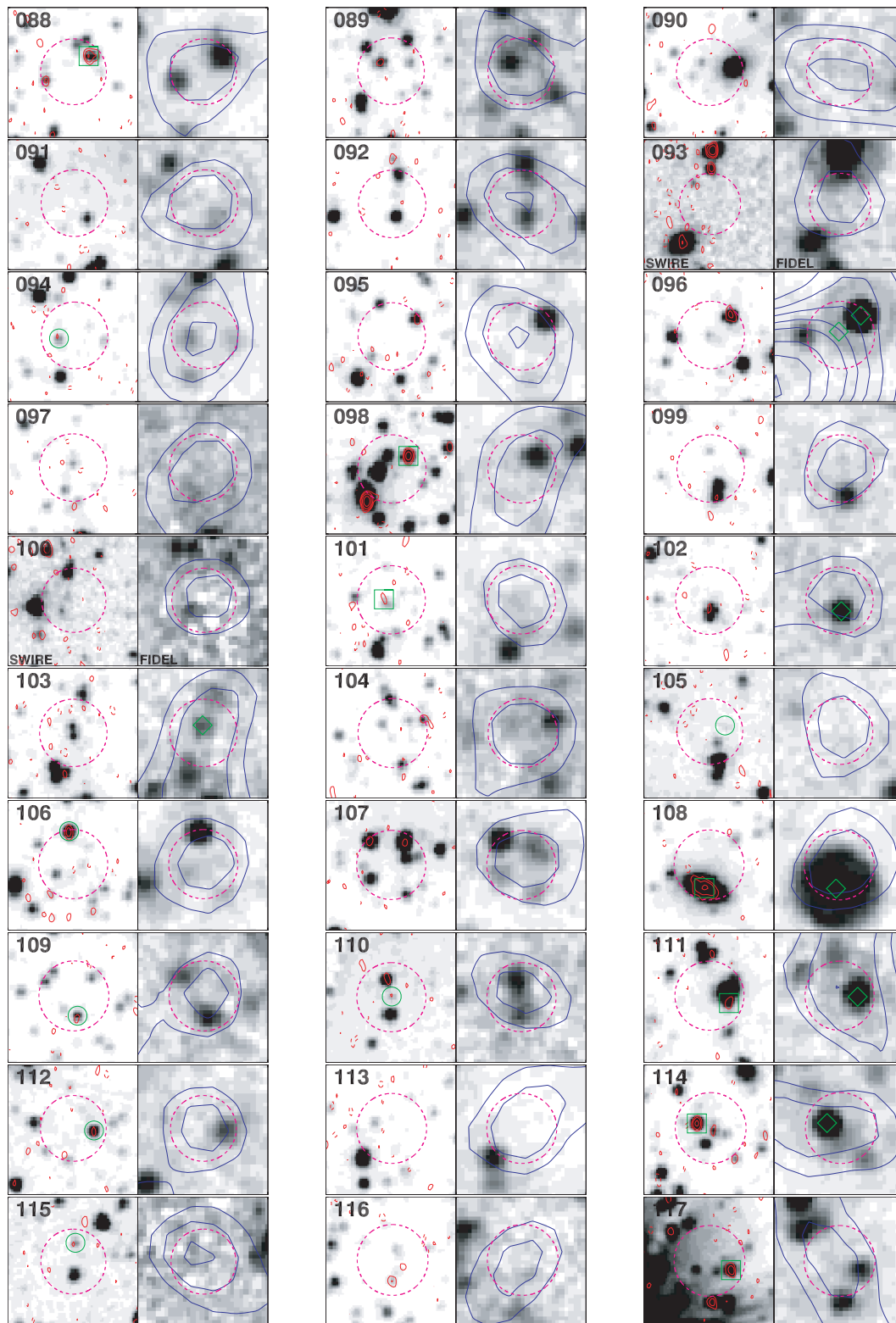


Figure A1 – continued

(LESS024) *LESS J033336.8–274401*: the secure radio counterpart is coincident with a $p < 0.1$ 24- μm source. A brighter radio source/24- μm source lies outside the search area at radio position 03:33:36.4418, $-27:43:55.671$.

(LESS026) *LESS J033136.9–275456*: no radio or 24- μm emission, but this source is a continuation of LESS004 and hence probably a blend. The radio/24- μm source to the south (03:31:36.9524, $-27:55:10.443$) is a possible contributor to this submm complex.

Figure A1 – *continued*

(LESS027) *LESS J033149.7–273432*: of the two robust IRAC counterparts, only the southern one has emission at $24\ \mu\text{m}$.

(LESS028) *LESS J033302.9–274432*: this source is a close neighbour of LESS059. There is no sign of any significant emis-

sion within the search radius. The nearest radio source beyond the search radius has a flux of $52\ \mu\text{Jy}$ at position $03:33:01.9865$, $-27:44:33.675$ and is associated with an obvious $24\text{-}\mu\text{m}$ source ($102\ \mu\text{Jy}$).

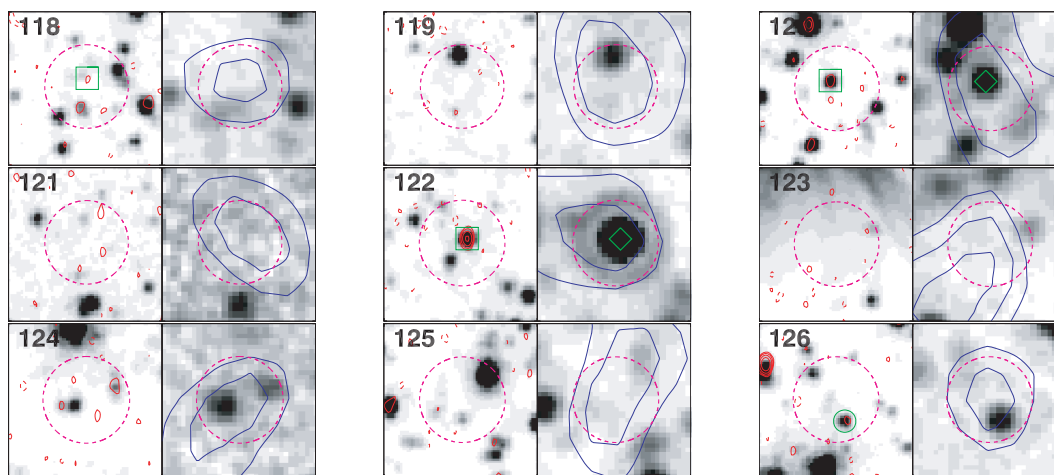


Figure A1 – continued

(LESS030) *LESS J033344.4–280346*: the radio sources to the north have positions 03:33:44.6396, $-28:03:38.273$ (240 μ Jy) and 03:33:44.9516, $-28:03:43.435$ (41 μ Jy).

(LESS031) *LESS J033150.0–275743*: this weak radio source has a p only slightly in excess of 0.05, is nearly coincident with a 24- μ m source and has a robust counterpart from the IRAC analysis.

(LESS033) *LESS J033149.8–275332*: this SMG is a close neighbour of LESS057.

(LESS034) *LESS J033217.6–275230*: this SMG merges into LESS010 and three 24- μ m sources lie along the line between the two SMGs. The nearby radio/24- μ m source has a position of 03:32:17.1874, $-27:52:21.074$ (93 μ Jy).

(LESS035) *LESS J033110.3–273714*: the 24- μ m emission is complex and the counterpart is difficult to see, but as the IRAC image reveals a faint source at the same position the DAOPHOT extraction seems to have been successful.

(LESS036) *LESS J033149.2–280208*: both radio and 24- μ m potential counterparts are coincidental and have $0.05 < p \leq 0.1$ and therefore we consider this a secure identification.

(LESS041) *LESS J033110.5–275233*: a pair of sources dominate the IRAC image, but only the one that is a robust identification has a counterpart at 24 μ m.

(LESS042) *LESS J033231.0–275858*: a radio/24- μ m source lies just to the north of the search radius at 03:32:31.4500, $-27:58:51.934$.

(LESS043) *LESS J033307.0–274801*: three 24- μ m sources cluster towards the centre of the submm emission and all three have weak radio emission. Only one is classified as a robust counterpart, based on the IRAC data.

(LESS046) *LESS J033336.8–273247*: this source is not covered by the 24- μ m FIDEL or SIMPLE 3.6- μ m data. The plots therefore show the shallower SWIRE data at each wavelength; at 24- μ m there is a clear counterpart to the robust radio identification.

(LESS047) *LESS J033256.0–273317*: the two IRAC robust counterparts may be a single, extended source; 24- μ m emission is centred closer to the western component.

(LESS049) *LESS J033124.4–275040*: three 24- μ m sources cluster towards the centre of the submm emission and all three have weak radio emission.

(LESS050) *LESS J033141.2–274441*: as with the previous SMG, a cluster of several (at least four) 24- μ m sources dominates the postage-stamp image and lie almost equidistant from the submm

centroid; one of them is a secure identification based on its radio emission. The secure 24- μ m identification at the very centre of the image is difficult to discern, but as a source is present at this position in the IRAC 3.6- μ m image we believe that it is real.

(LESS052) *LESS J033128.5–275601*: this SMG is a close neighbour of LESS075.

(LESS058) *LESS J033225.8–273306*: very weak 24- μ m emission that is not present in either the DAOPHOT or APEX catalogues is coincident with a $p = 0.06$ radio source.

(LESS060) *LESS J033317.5–275121*: the $p < 0.1$ radio source to the south is coincident with a $p < 0.1$ 24- μ m source and we consider this a secure identification.

(LESS063) *LESS J033308.5–280044*: the extremely weak radio emission that has been classed as a secure identification by the p -statistic is not seemingly associated with any 24- μ m emission, and we warn that it may be spurious. We do not include it in the redshift analysis.

(LESS066) *LESS J033331.7–275406*: this is a close neighbour to LESS123.

(LESS067) *LESS J033243.3–275517*: three 24- μ m sources cluster towards the centre of the submm emission and all three have weak radio emission; one is a secure counterpart.

(LESS068) *LESS J033233.4–273918*: the nearest radio source beyond the search radius has a position of 03:32:33.5615, $-27:39:28.892$, a flux of 50 μ Jy and is offset by 10.5 arcsec from the nominal submm position.

(LESS071) *LESS J033306.3–273327*: increasing the search radius by a modest 0.4 arcsec would lead to the identification of a $p < 0.05$ radio counterpart (200 μ Jy at 03:33:05.6632, $-27:33:28.666$) with a coincident 24- μ m source.

(LESS073) *LESS J033229.3–275619*: the radio $p < 0.05$ identification is very weak, but is coincident with a very weak 15.2- μ Jy 24- μ m source that lies beneath the 3.5σ catalogue threshold.

(LESS074) *LESS J033309.3–274809*: we find two IRAC robust counterparts separated by only a few arcsec. One is robust based on the IRAC p -statistic alone whilst the other is robust due to $p < 0.1$ for both the IRAC and the radio maps.

(LESS075) *LESS J033126.8–275554*: this is a close neighbour of LESS052.

(LESS076) *LESS J033332.7–275957*: the submm emission to the north of this source is LESS015.

(LESS082) *LESS J033253.8–273810*: a pair of 24- μ m sources align with the elongation of the submm emission.

(LESS085) *LESS J033110.3–274503*: the radio source just outside the search radius has a position of 03:31:09.7733, –27:45:08.625, a flux of 46 μ Jy and is offset by 8.7 arcsec from the nominal submm position.

(LESS086) *LESS J033114.9–274844*: the radio source just outside the search radius has a position of 03:31:14.1207, –27:48:44.229 (J2000), a flux of 102 μ Jy and is offset by 10.3 arcsec from the nominal submm position.

(LESS087) *LESS J033251.1–273143*: there are two radio counterparts, only one of which has 24- μ m emission. This may be a radio core and jet.

(LESS096) *LESS J033313.0–275556*: this SMG lies very close to LESS001. The secure 24- μ m identification at the very centre of the image is difficult to discern and appears to be part of the Airy ring, but an IRAC 3.6- μ m source at this position again confirms that the DAOPHOT extraction is reliable.

(LESS098) *LESS J033130.2–275726*: two radio sources align themselves closely with the submm elongation. The southern of the pair has a flux of 368 μ Jy and a position of 03:31:30.7540, –27:57:35.129 (J2000).

(LESS103) *LESS J033325.3–273400*: this SMG is a close neighbour of LESS111.

(LESS107) *LESS J033130.8–275150*: a group of five catalogued

24- μ m sources within the search radius form a ring around the submm position, two of which have associated weak radio emission.

(LESS110) *LESS J033122.6–275417*: the very faint IRAC identification also has a counterpart in a complex 24- μ m structure that DAOPHOT disentangles into three separate components.

(LESS111) *LESS J033325.6–273423*: this SMG is a close neighbour of LESS103. It has a robust counterpart in both the radio and the MIPS catalogues, but the weaker radio component is significantly offset (2 arcsec) from the much brighter MIPS detection. This perhaps suggests that the radio source is spurious, but its relatively high S/N (>5) argues that it is unlikely to be a false detection.

(LESS117) *LESS J033128.0–273925*: there is a striking alignment of five 24- μ m sources with the elongation of the submm emission along 30° , several of which have associated radio emission.

(LESS118) *LESS J033121.8–274936*: the extremely weak radio emission that has been classed as a secure identification by the p -statistic is not seemingly associated with any MIPS or IRAC emission, and we warn that it may be spurious. We do not include it in the redshift analysis.

(LESS123) *LESS J033330.9–275349*: this is a close neighbour to LESS066.

This paper has been typeset from a \TeX/L\AA\TeX file prepared by the author.